



# WaveComBE

mmWave Communications in the Built Environments

## WaveComBE\_D3.3

Recommendation on joint optimization of  
mm-Wave small-cell deployment and the  
built environments

Version Final

Date: 30/09/2021

## Document properties:

<b>Grant Number:</b>	766231
<b>Document Number:</b>	D3.3
<b>Document Title:</b>	Recommendation on joint optimization of mm-Wave small-cell deployment and the built environments
<b>Partners involved:</b>	USFD, UDUR, UT, LTV, RPN, UPV
<b>Authors:</b>	Yixin Zhang, Chen Chen, Danaisy Prado-Alvarez, Monika Drozdowska, Chunxia Qin, Narcís Cardona, Jose F. Monserrat, Frederik Naessens, Xiaoli Chu, Jie Zhang
<b>Contractual Date of Delivery:</b>	30/09/2021
<b>Dissemination level:</b>	PU <sup>1</sup>
<b>Version:</b>	Final
<b>File Name:</b>	WaveComBE D3.3

---

<sup>1</sup> CO = Confidential, only members of the consortium (including the Commission Services)

PU = Public

## Table of contents

Table of contents.....	3
Executive Summary .....	5
List of Figures .....	7
List of Tables.....	9
List of Acronyms and Abbreviations.....	10
1. Introduction .....	12
2. On the Performance of Indoor Multi-Story Small-Cell Networks .....	13
2.1. Network model.....	13
2.2. Coverage Probability .....	14
2.3. Effect of Small-cell BS Density .....	15
2.4. Effect of Story Height .....	15
2.5. Effect of the Penetration Loss of the Ceiling.....	16
2.6. Recommendation .....	16
3. Joint Optimization of Indoor MmW MIMO Small-cell Deployment and Hybrid Beamforming.....	17
3.1. System Model.....	17
3.2. Hybrid Beamforming .....	18
3.3. Optimization Objective and Formulation.....	18
3.4. Joint Optimization of Small-cell Deployment and Hybrid Beamforming .....	19
3.5. Performance Comparison of Single-cell Scenario and Two-cell Scenario.....	20
3.6. Recommendation .....	21
4. Optimising the Wireless Friendliness of Indoor Building Materials.....	22
4.1 System Model.....	22
4.2 Channel Capacity .....	26
4.2.1 The Distribution of the Squared Singular Value of Channel .....	26
4.2.2 Closed-form Ergodic Capacity .....	29
4.3 Wireless Friendliness Evaluation Scheme .....	29
4.4 Numerical Results.....	31
4.4.1 The Ergodic Capacity of a Specific Sample Point.....	32
4.4.2 The Ergodic Capacity Distribution in a Square Room.....	33
4.4.3 The Impact of Wall Permittivity and Thickness on Spatially Averaged Capacity .....	35
4.5 Recommendation .....	37
5. System-level Mm-Wave Small-cell Simulator based on iBuildNet.....	38

5.1.	Outdoor Environment Modelling .....	38
5.2.	Indoor Environment Modelling .....	38
5.3.	User Modelling and Traffic Map.....	39
5.4.	Simulation Result in Real Scenarios .....	40
5.5.	Recommendation .....	44
6.	Sensitivity Analysis of Built Environment Modelling Realism .....	45
6.1.	Presentation of the Scenario.....	45
6.2.	Different Accuracy Levels in the Scenario Modelling.....	46
6.3.	Analysis and Numerical Results.....	47
6.4.	Recommendation .....	48
7.	Conclusions .....	49
	References.....	50

## Executive Summary

The usage of the wireless services increases, thus the bandwidth available for the fifth generation (5G) at millimeter waves (mmW) frequencies gets more attention than before. There are some new scenarios that have never been considered in the previous generations and require additional guidelines in the deployment. This document provides recommendations on joint optimization mmW small-cells deployment and on the built environment.

Mobile data traffic has been largely generated indoors. However, indoor cellular networks have been studied either on a two-dimensional (2D) plane or as an intractable optimization problem for a multi-story building. In this deliverable, we develop a tractable three-dimensional small-cell network model for a multi-story building. On each story, the small-cell base stations (BS) are distributed following a 2D homogeneous Poisson point process. We analytically derive the downlink coverage probability for the indoor network as functions of the story height, the penetration loss of the ceiling and the BS density. Our tractable expressions show that a higher penetration loss of the ceiling leads to a higher coverage probability. Meanwhile, with the increase of the story height or the BS density, the downlink coverage probability first decreases and then increases after reaching a minimum value, indicating that certain values of story height and BS density should be avoided for good indoor wireless coverage.

MmW communication achieves multi-Gbps data rates by taking advantage of the large bandwidth in the mmW spectrum. Due to the short link distance and weak penetration loss through walls, it is a natural choice to deploy mmW small cells in indoor hotspots. On the other hand, due to the high hardware complexity and power consumption of the mmW spectrum, it is necessary to appropriately design hybrid analog and digital beamforming. In this deliverable, we jointly optimize the deployment of mmW small-cells and their hybrid beamforming patterns to maximize the sum user rate/minimum user rate in a meeting room. We find the optimal locations of small-cells maximizing the network performance metrics using greedy search and evaluate the performance of four typical digital precoders: unit matrix, MRT, ZF and MMSE.

The tremendous popularity of internet of things (IoT) applications and wireless devices have prompted a massive increase of indoor wireless traffic. To further explore the potential of indoor IoT wireless networks, creating constructive interactions between indoor wireless transmissions and the built environments becomes necessary. The electromagnetic (EM) wave propagation indoors would be affected by the EM and physical properties of the building material, e.g., its relative permittivity and thickness. In this paper, we construct a new multipath channel model by characterising wall reflection (WR) for an indoor line-of-sight (LOS) single-user multiple-input multiple-output (MIMO) system and derive its ergodic capacity in closed-form. Based on the analytical results, we define the wireless friendliness of a building material based on the spatially averaged indoor capacity and propose a scheme for evaluating the wireless friendliness of building materials. Monte Carlo simulations validate our analytical results and manifest the significant impact of the relative permittivity and thickness of a building material on indoor capacity, indicating that the wireless friendliness of building materials should be considered in the planning and optimisation of indoor wireless networks. The outcomes of this paper would enable appropriate selection of wall materials during building design, thus enhancing the capacity of indoor LOS MIMO communications.

The environment has a significant impact on wireless propagation in the mmW band, therefore the scenarios should be as close to reality as possible during modeling. In Ranplan Professional, which is based on iBuildNet, outdoor and indoor scenarios may be considered. For outdoor an Outdoor Layout Module was proposed and integrated, while for indoor there are proposed some ways for importing data. Except of the environment and the network model for simulations the user and the traffic map should be modelled. When they are considered, the simulation can provide accurate performance prediction for the deployment of the system, especially for heterogeneous wireless access networks.

In the mmW bands, given the small wavelengths used and the large propagation losses, there are propagation phenomena that become more relevant such as diffuse scattering and diffraction and other phenomena that become less perceptible such as transmission. Taking into account the above and using as a tool a channel simulator developed at the UPV, this paper shows the evaluation results of the impact on mmW of the accurate recreation of real scenarios taking into account both the building materials and the presence of furniture in indoor scenarios. These results are analyzed, concluding that the characterization of materials and the consideration of furniture do have a considerable effect on the channel estimation. This effect is more noticeable in cases where the main propagation path is reflections or diffraction, i.e., there is no direct line of sight.

**Disclaimer:** This work has been performed in the framework of the H2020 project WaveComBE (Grant agreement ID: 766231) co-funded by the EU. This information reflects the consortium's view, but the consortium is not liable for any use that may be made of any of the information contained therein. This deliverable has been submitted to the EU commission, but it has not been reviewed and it has not been accepted by the EU commission yet.

## List of Figures

- Fig. 2-1. An illustration of the small-cell network in a multi-story building.
- Fig. 2-2. The coverage probability vs. the BS density.
- Fig. 2-3. Coverage probability vs. the story height and BS density.
- Fig. 2-4. The coverage probability vs. the ceiling penetration loss  $w$ .
- Fig. 3-1. An illustration of the meeting room.
- Fig. 3-2. Sum user rate versus cell location.
- Fig. 4-1. The LOS path and the WR path between indoor BS and UE.
- Fig. 4-2. Cartesian coordinates for a room, e.g.,  $W = L = 10$  m, where the BS is close to the considered wall and there is an L-shaped route inside.
- Fig. 4-3. The MPDF of an unordered squared singular value at the three points, for  $\zeta = 0.2$ ,  $\varepsilon = 5.31 - j0.5861f^{-0.1905}$ . Markers represent simulation values while lines represent analytical values.
- Fig. 4-4. Relationship between ergodic capacity and transmit SNR at three points, for  $\zeta = 0.2$ ,  $\varepsilon = 5.31 - j0.5861f^{-0.1905}$ . Markers represent simulation values while lines represent analytical values.
- Fig. 4-5. Fig. 4-5 Ergodic capacity at the points for L-shaped route, for  $\zeta = 0.2$ ,  $\varepsilon = 5.31 - j0.5861f^{-0.1905}$ .
- Fig. 4-6. Ergodic capacity distribution in the 10 m 10 m square room, for dB, , . Markers represent simulation values while the lines represent analytical values.
- Fig. 4-7. The ergodic capacity difference between our proposed channel and the Rician channel, for  $\rho_T = 60$  dB,  $\zeta = 0.2$ ,  $\varepsilon = 5.31 - j0.5861f^{-0.1905}$ . The positive/negative difference indicates constructive/destructive interference.
- Fig. 4-8. Impact of wall permittivity on spatially averaged capacity for  $\rho_T = 60$  dB.
- Fig. 4-9. Impact of wall thickness on spatially averaged capacity for  $\rho_T = 60$  dB.
- Fig. 4-10. The composite impact of permittivity and thickness on spatially averaged capacity for  $\rho_T = 60$  dB.
- Fig. 5-1. 3D view of an outdoor environment modelling.
- Fig. 5-2. 3D view of an indoor environment modelling.
- Fig. 5-3. User terminal modelling.
- Fig. 5-4. Traffic map.
- Fig. 5-5. Import GIS Data window in Ranplan Professional.

Fig. 5-6. 3D view of the imported GIS data (central London).

Fig. 5-7. Supported KPIs in 5G NR.

Fig. 5-8. 2D view of outdoor SS RSRP in the whole area.

Fig. 5-9. 3D view of outdoor SS RSRP.

Fig. 5-10. 2D view of outdoor SS RSRP in the hotspots area.

Fig. 5-11. Traffic Map of 30 Users in the hotspots.

Fig. 5-12. 2D view of effective user throughput in the hotspots area.

Fig. 6-1. Top view of the Meeting Room created in the simulation tool.

Fig. 6-2. Photo of the Meeting Room at Durham University.

Fig. 6-3. Top view of the Meeting Room with Tx in the corner and Rx's' locations around the table.

Fig. 6-4. Received power for the 16 RX positions.



## List of Tables

Table 3-1. Maximum sum user rate

Table 3-2. Maximum minimum user rate

Table 4-1. Main simulation assumptions

## List of Acronyms and Abbreviations

2D	Two-dimensional
3D	Three-dimensional
5G	Fifth Generation
AoA	Angle of Arrival
AoD	Angle of Departure
ASE	Area Spectral Efficiency
BE	Built Environment
BS	Base Station
EM	Electromagnetic
FM CW	Frequency Modulated Continuous Wave
HPBW	Half Power Beam Width
IoT	Internet of Things
LOS	Line-Of-Sight
LTE	Long Term Evolution
MIMO	Multiple Input Multiple Output
MMSE	Minimum Mean Squared Error
MP	Multipath
MRT	Maximum Radio Transmission
NLOS	Non-Line-Of-Sight
NSA	Non-Standalone
NR	New Radio
PPP	Poisson Point Process
RF	Radio Frequency
RMS DS	Root Mean Square Delay Spread
RSRP	Reference Signal Received Power
SA	Standalone
SCN	Small Cell Network
SINR	Signal-to-Interference-plus-Noise Ratio
SNR	Signal-to-Noise Ratio

TE	Transverse Electric
TM	Transverse Magnetic
ULA	Uniform Linear Array
UE	User Equipment
WR	Wall Reflection
ZF	Zero-Forcing

## 1. Introduction

Nowadays, mmW communication is more and more popular. It is seen as a solution for many problems in wireless communication in lower bands. First of all, the mmW band is not so crowded, thus there is a lot of space for new services. There are some bands that are unlicensed worldwide for which standards are created. For example IEEE 802.11ad, and IEEE 802.11ay for 60 GHz band. According to 5G NR, services in the mmW band will have a lower delay, and higher data rate, compared to those provided in 4G. Secondly, using small cells and macrocells, the coverage of the network will be better located. That proves that using mmW communication is perfect for indoor environments, where there is a lot of people in a wide area using many different services.

However, due to the special scenarios, and the closed nature of the built environments, there is a lot of challenges in network optimization and deployment. The environment is closed, with different dimensions and materials used for walls, ceiling, and floor. It may be empty or full of movable obstacles. In some environments people can walk inside, in some they are static, and in some, there are no people. Buildings may have one or multiple stores. All those things, and many more, have an impact on the network. They should be considered before we start to plan our network and evaluate during the whole process of network optimisation and deployment. Taking that into consideration in this document we give some recommendations regarding the aforementioned characteristics of the built environment.

Chapter 2 gives recommendations for multi-store buildings. In Chapter 3 joint optimization of Indoor mmW MIMO small-cell deployment and hybrid beamforming is discussed. Recommendations regarding materials used in indoor environments are given in Chapter 4. Chapter 5 provides guidelines for a system-level mmW small-cell simulator based on iBuildNet. Environment modeling is described in Chapter 6. Finally, Chapter 7 contains some conclusions based on recommendations from each chapter.

## 2. On the Performance of Indoor Multi-Story Small-Cell Networks

### 2.1. Network model

We consider a building with  $2M + 1$  stories, where  $M \geq 1$ . As shown in Fig. 2-1, all the stories from the ground story to the top story are numbered from  $-M$  to  $M$ , respectively, and we assume that the typical user equipment (UE) is located on the 0th story. The base station (BS) height and the UE height are assumed to be  $h_B$  and  $h_U$ , respectively. The height for each story is denoted by  $H$ , which includes the ceiling height and the ceiling thickness. For the  $j$ th story, the small-cell BSs are randomly distributed following a homogeneous Poisson point process (PPP)  $\phi_j$  with intensity  $\lambda$  BSs/m<sup>2</sup> and UEs are also PPP distributed with a density of  $\rho$  UEs/m<sup>2</sup>. For simplicity, we assume that the values of  $\lambda$  and  $\rho$  do not change across different stories. For the downlink cellular network, we assume that the desired and interference signals experience the distance dependent path loss, where the same path loss exponent  $\alpha$  is used for all the stories. Small scale fading is modeled as Rayleigh fading with an unit average power for all the channels [1]. For analytical tractability, in the following, we assume that on each story,  $h_B = h_U$ . Note that under this assumption, the value of  $h_B$  and  $h_U$  has no effect on the coverage probability.

One UE can only be associated to one BS. We use  $m \in \{-M, -(M-1), \dots, 0, 1, \dots, M\}$  as the index of the story that contains the serving BS for the typical UE. Let  $R_m$  denote the horizontal distance from the nearest BS on the  $m$ th story to the typical UE, and then the distance from the nearest BS on the  $m$ th story to the typical UE is given by

$$l_m = \sqrt{(mH)^2 + R_m^2}. \quad (2-1)$$

The UE is associated to the BS providing the strongest downlink received signal. The average power of the strongest received signal from a BS on the  $m$ th story is given by [2]

$$P_{r,m} = P\beta_0 l_m^{-\alpha} w^{|m|}, \quad (2-2)$$

where  $P$  is the transmit power of a BS,  $\beta_0$  is the path loss at the reference distance of 1 m,  $w$  ( $0 < w < 1$ ) is the penetration loss of one ceiling, and the power of the small scale fading is averaged to be 1.

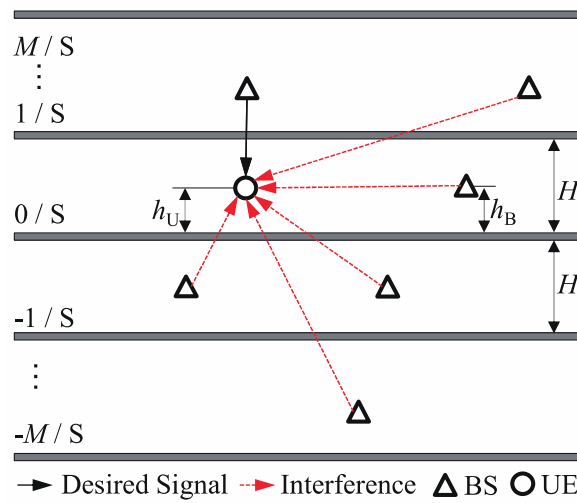


Fig. 2-1. An illustration of the small-cell network in a multi-story building.

## 2.2. Coverage Probability

The coverage probability  $C$  is the probability that the Signal-to-Interference-plus-Noise Ratio (SINR) of the typical UE is higher than a target threshold  $T$ . The typical UE can be connected to at most one BS, so the coverage probability is given by

$$C = \sum_{m=-M}^M C_m B_m, \quad (2-3)$$

where  $B_m$  is the probability that the typical UE associates to the BS on the  $m$ th story, and  $C_m$  is the corresponding coverage probability. Since  $C_m = C_{-m}$ , for clarity, we consider  $0 \leq m \leq M$ ,  $C$  will be

$$C = C_0 B_0 + 2 \sum_{m=1}^M C_m B_m, \quad (2-4)$$

where

$$C_m = \sum_{k=m}^M C_{m,k}, \quad (2-5)$$

where

$$C_{m,k} = \frac{2\pi\lambda}{B_m} \int_{I_{m,k}}^{I_{m,(k+1)}} x \exp\left\{-\frac{T}{\text{SNR}_m} - \pi\lambda(F_m + F_{m,k}) - \pi\lambda Q(m^2 H^2 + x^2) w^{-\frac{2m}{\alpha}} - 2\pi\lambda(m^2 H^2 + x^2) \int_{n=1}^M Q_{m,n,k} w^{-\frac{2}{\alpha}(n-m)}\right\} dx, \quad (2-6)$$

$$\text{where } I_{m,k} = \begin{cases} \sqrt{(kH)^2 w^{\frac{2(m-k)}{\alpha}} - (mH)^2}, & m \leq k \leq M \\ \infty, & k = M + 1 \end{cases}$$

$$F_m = 2 \left( (m^2 H^2 + x^2) \frac{w^{-\frac{2}{\alpha}} \left(1 - w^{-\frac{2(m-1)}{\alpha}}\right)}{1 - w^{-\frac{2}{\alpha}}} - \frac{(m-1)m(2m-1)}{6} H^2 \right) + (m^2 H^2 + x^2) w^{-\frac{2m}{\alpha}} + 2x^2,$$

$$F_{m,k} = 2 \left( (m^2 H^2 + x^2) \frac{w^{-\frac{2}{\alpha}} \left(1 - w^{-\frac{2(k-m)}{\alpha}}\right)}{1 - w^{-\frac{2}{\alpha}}} - \frac{k(k+1)(2k+1)(m-1)m(2m-1)}{6} H^2 \right),$$

$$\text{SNR}_m = \frac{P_W^m \beta_0 (m^2 H^2 + x^2)^{-\frac{\alpha}{2}}}{N}, \quad Q = \frac{2T}{\alpha-2} \times {}_2F_1\left[1, 1 - \frac{2}{\alpha}; 2 - \frac{2}{\alpha}; -T\right], \text{ and}$$

$$Q_{m,n,k} = \begin{cases} Q, & n \leq k \\ \frac{2TB_{m,n,x}^{\frac{2}{\alpha}-1}}{\alpha-2} \times {}_2F_1\left[1, 1 - \frac{2}{\alpha}; 2 - \frac{2}{\alpha}; -\frac{T}{B_{m,n,x}}\right], & n > k \end{cases}$$

$$\text{where } B_{m,n,x} = (nH)^\alpha w^{m-n} (m^2 H^2 + x^2)^{-\frac{\alpha}{2}}.$$

### 2.3. Effect of Small-cell BS Density

The default values of parameters are set as  $\beta_0 = -38.5\text{dB}$ ,  $T = 0\text{ dB}$ ,  $P = 33\text{ dBm}$ ,  $\alpha = 4$ ,  $H=3\text{ m}$ ,  $\lambda = 0.01\text{BS/m}^2$ . To better demonstrate the performance of the multi-story small-cell network (SCN), we ignore the thermal noise and set  $w$  as  $-10\text{ dB}$ . It is well-known that the BS density does not affect the network coverage probability in interference-limited networks and the area spectral efficiency (ASE) scales linearly with the network densification [3]. This is because the increased interference can be compensated by the shrunken distance between the typical UE and the connected BS. However, we observe a different scaling law in our proposed multi-story SCN model. In Fig. 2-2, we analyze the influence of the BS density per story to the coverage probability for  $H = 3\text{ m}$ ,  $H = 4\text{ m}$ ,  $H = 5\text{ m}$  [4], respectively. Note that the  $M = 0$  curve stands for the two-dimensional (2D) scenario and its coverage probability remains unchanged with the increase of the BS density. When  $M = 1$ , the coverage probability first decreases and then increases back with the network densification. This phenomenon is referred to as the Coverage Probability Chasm hereafter. To alleviate the performance loss, it is necessary to avoid the Chasm area in the practical deployment of BSs.

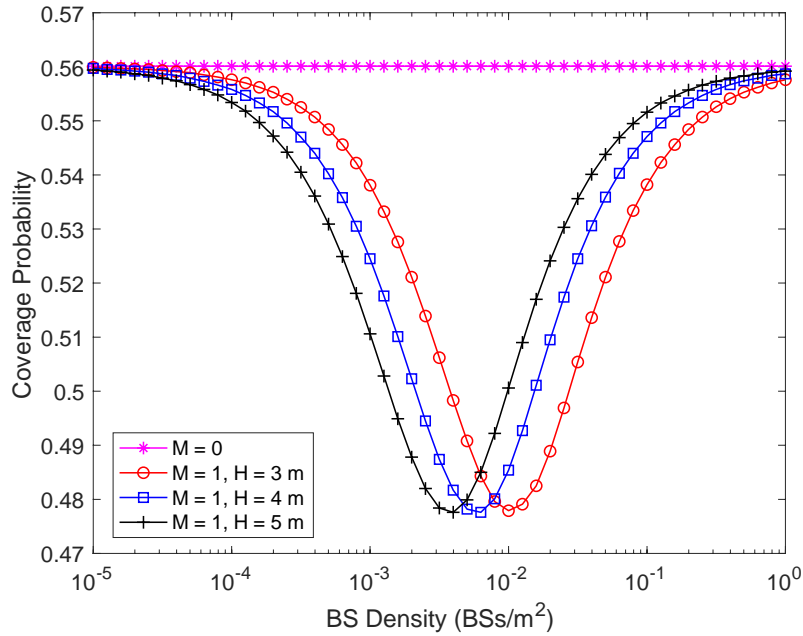


Fig. 2-2. The coverage probability vs. the BS density.

### 2.4. Effect of Story Height

In Fig. 2-3, we assume that the penetration loss of the ceiling  $w = -5\text{ dB}$ , and the threshold of the coverage probability is  $0\text{ dB}$ . We assume that the BS height and UE height are both  $1.2\text{ m}$ , so the minimum story height is  $1.2\text{ m}$ . We plot the three-dimensional (3D) figure to show the influence of the story height with different BS densities, where a conspicuous Coverage Probability Chasm can be observed. For most of the BS densities, the coverage probability of the typical UE first decreases and then increases with the increasing story height. Due to the existing of the Coverage Probability Chasm, there is a worst story height that leads to the lowest coverage probability. The worst story height is affected by the BS density, as can be seen, when the BS density increases, the worst story height decreases.

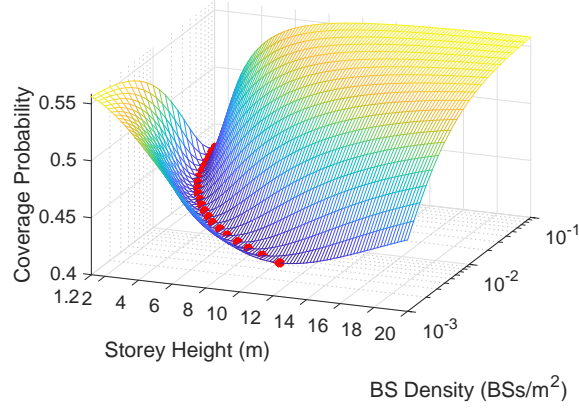


Fig. 2-3. Coverage probability vs. the story height and BS density.

### 2.5. Effect of the Penetration Loss of the Ceiling

In Fig. 2-4, we analyze the influence of the penetration loss of the ceiling (in linear scale). Larger  $w$  means smaller penetration loss. It is observed that the coverage probability increases with stronger penetration loss, which indicates that the cross-story communication is harmful to the network performance when the BSs and UEs share the same height. When  $w = 0$ , the typical UE only connects to the BSs on the 0th story, so the network performance is the same with the 2D model. According to this conclusion, we should choose the materials with higher penetration loss for the ceilings of a new building.

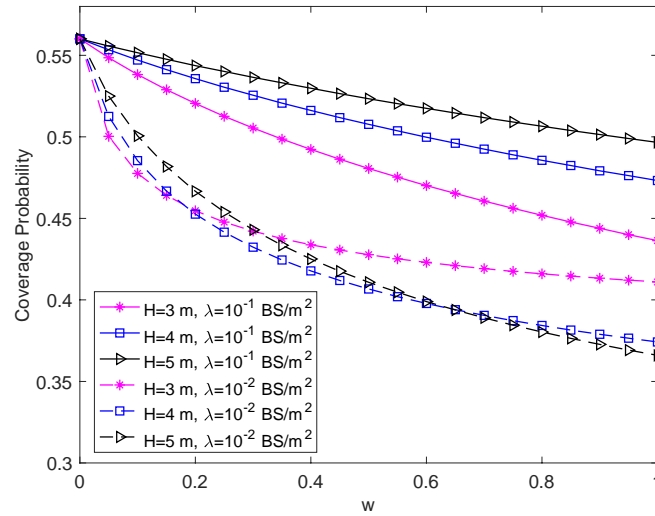


Fig. 2-4. The coverage probability vs. the ceiling penetration loss  $w$ .

### 2.6. Recommendation

We have presented a novel theoretical discovery, i.e., the Coverage Probability Chasm. The coverage probability of the SCN in a multi-story building first decreases and then increases with the increase of the story height and the network density. Accordingly, we identify a range of story heights associated with poor network performance that should be avoided in the design of a new building. Moreover, we show that the setting of BS density per story in a multi-story building should avoid the values that result in poor coverage. In addition, we show that a ceilings with a higher penetration loss can provide a better network performance. The contributions of this paper can shed insight on the design of new buildings and future indoor SCN deployments.



### 3. Joint Optimization of Indoor MmW MIMO Small-cell Deployment and Hybrid Beamforming

#### 3.1. System Model

We consider the deployment of mmW MIMO small-cells in a meeting room, as shown in Fig. 3-1<sup>2</sup>. The length, width and height of the room are 8.8 m, 5.7 m and 3.5 m, respectively. We aim to maximize the downlink transmission performance of a mmW MIMO system consisting of  $L$  small-cells and  $K$  UEs. Since mmW frequencies suffer from higher penetration loss through blockages than micro-wave frequencies [5][6], the small-cells are mounted on the ceiling for easy deployment and higher Line-Of-Sight (LOS) probability.

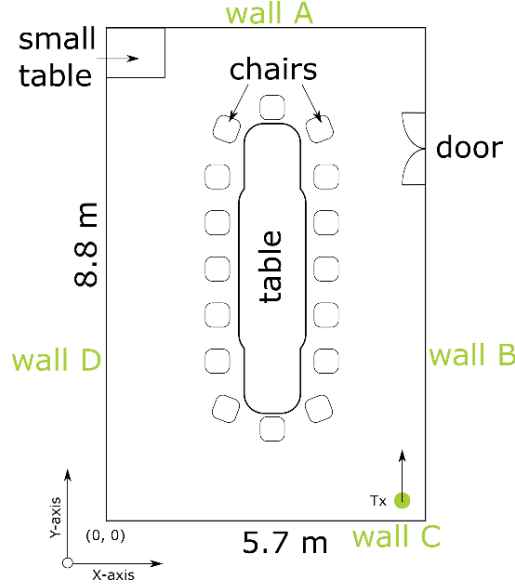


Fig. 3-1. An illustration of the meeting room.

Each small-cell is equipped with a uniform linear array (ULA) with  $M_t$  antennas, while each UE has a single antenna. The channels are characterized by using the extended Saleh-Valenzuela geometric channel model [7]. The channel between small-cell  $l$  and UE  $k$  is defined as

$$\mathbf{h}_{kl} = \sum_{p=1}^{N_p} \lambda_{p,k,l} \mathbf{a}(M_t, \theta_{p,k,l}), \quad (3-1)$$

where  $N_p$  is the number of paths,  $\lambda_{p,k,l}$  is the channel gain coefficient of path  $p$  between small-cell  $l$  and UE  $k$ ,  $\theta_{p,k,l}$  is the horizontal angle of departure (AoD) of path  $p$  between small-cell  $l$  and UE  $k$ , and  $\mathbf{a}(M_t, \theta_{p,k,l})$  is the steering vector function defined as

$$\mathbf{a}(M_t, \theta_{p,k,l}) = [1, e^{j\pi \cos(\theta_{p,k,l})}, e^{j2\pi \cos(\theta_{p,k,l})}, \dots, e^{j\pi(M_t-1)\cos(\theta_{p,k,l})}]^H. \quad (3-2)$$

We assume that LOS paths are always available between the cells and UEs. For mmW channels containing LOS components, the effect of non-Line-Of-Sight (NLOS) signals is negligible since the channel gains of NLOS paths are typically 20 dB weaker than those of LOS signals [8]. Hence, in the following, we will focus on LOS paths, i.e.,  $N_p = 1$ . For the LOS link, the channel gain coefficient  $\lambda_{1,k,l}$  is a constant, depending on the propagation loss affected by propagation distance and carrier frequency, which is expressed as [9]

<sup>2</sup> This figure was plotted by Miss Monika Drozdowska for the channel measurements at Durham University.

$$\lambda_{1,k,l} = \frac{1}{\left(\frac{4\pi f}{c}\right) d_{k,l}^\alpha}, \quad (3-3)$$

where  $d_{k,l}^\alpha$  is the distance from small-cell  $l$  to UE  $k$ ,  $\alpha$  is the path loss exponent,  $f$  is the carrier frequency,  $c$  is the constant of light speed.

### 3.2. Hybrid Beamforming

To achieve a balance between energy consumption and beamforming gain, we adopt hybrid beamforming [10]. Consider a hybrid beamforming case where  $M_{rf}$  is the number of radio frequency (RF) chains at a cell. The radio frequency (analog) and baseband (digital) precoders at cell  $l$  are given by  $\mathbf{U}_l = [\mathbf{u}_{1l} \dots \mathbf{u}_{M_{rf}l}] \in \mathbb{C}^{M \times M_{rf}}$  and  $\mathbf{V}_l = [\mathbf{v}_{1l} \dots \mathbf{v}_{K_l l}] \in \mathbb{C}^{M_{rf} \times K_l}$ , respectively, where  $K_l$  is the number of UEs served by cell  $l$ . In general,  $M_t \geq M_{rf} \geq K_l$ . We assume  $M_{rf} = K_l$  so the system can generate a different signal for each UE. When all the cells operate in the same frequency band, the received signal at UE  $k$  of cell  $l$  during the data transmission phase is given by

$$\begin{aligned} y_{kl} &= \sqrt{\frac{P}{K_l}} \sum_{j=1}^L \sum_{i=1}^{K_j} \mathbf{h}_{kl}^H \mathbf{U}_j \mathbf{v}_{ij} s_{ij} + n_k \\ &= D_{kl} + I_{kl} + n_k, \end{aligned} \quad (3-4)$$

where  $D_{kl} = \sqrt{\frac{P}{K_l}} \mathbf{h}_{kl}^H \mathbf{U}_l \mathbf{v}_{kl} s_k$  is the desired signal,  $I_{kl} = \sqrt{\frac{P}{K_l}} \sum_{j=1}^L \sum_{i=1}^{K_j} \mathbf{h}_{kl}^H \mathbf{U}_j \mathbf{v}_{ij} s_{ij} - D_{kl}$  is the interference signal,  $P$  is the transmit power of a cell,  $s_{ij}$  is the unit-power data signal and  $n_k \sim \mathcal{CN}(0, \sigma_n^2)$  is the noise at UE  $k$ .

#### 3.2.1. Analog Beamforming

We optimize the analog precoder to maximize the desired signal received by each UE through assuming that  $\mathbf{V}_l$  is a unit matrix. Under this assumption,  $|D_{kl}|^2 = |\mathbf{h}_{kl}^H \mathbf{u}_{kl}|^2$ , which can be maximized by setting  $\mathbf{u}_{kl} = \mathbf{a}(M_t, \theta_{p,k,l})$  [8].

#### 3.2.2. Digital Beamforming

In this deliverable, four digital precoders are investigated: unit matrix, maximum-ratio transmitter (MRT), zero-forcing (ZF) and minimum mean squared error (MMSE). Defining that

$$\mathbf{H}_l = \begin{bmatrix} \mathbf{h}_{1l}^H \mathbf{U}_l \\ \dots \\ \mathbf{h}_{K_l l}^H \mathbf{U}_l \end{bmatrix}, \text{ at cell } l, \text{ MRT precoder is given by } \mathbf{V}_l^{\text{MRT}} = \mathbf{H}_l^H, \text{ ZF precoder is given by } \mathbf{V}_l^{\text{ZF}} =$$

$\mathbf{H}_l^H (\mathbf{H}_l \mathbf{H}_l^H)^{-1}$ , and MMSE precoder is given by  $\mathbf{V}_l^{\text{MMSE}} = \mathbf{H}_l^H \left( \frac{P}{K_l} \mathbf{H}_l \mathbf{H}_l^H + \sigma_n^2 \mathbf{I}_{K_l} \right)^{-1}$ , where  $\mathbf{I}_{K_l}$  is an unit matrix. Notice that  $\mathbf{H}_l$  may be a low-rank matrix for some cell locations that lead to some of the UEs having the same AoD. For these locations,  $\mathbf{V}_l^{\text{ZF}}$  cannot be calculated and instead we use the unit matrix as the precoder.

### 3.3. Optimization Objective and Formulation

We focus on two optimization objectives: sum user rate and minimum user rate. Then our optimization problems can be formulated as

$$\begin{aligned} \text{P1: } & \max_{\Omega, \Theta} \sum_{l=1}^L \sum_{k=1}^{K_l} r_{kl}, \\ \text{s. t. } & 0 \leq x_l \leq 5.7, 0 \leq y_l \leq 8.8, 1 \leq l \leq L, \end{aligned} \quad (3-5)$$

and

$$\begin{aligned}
\text{P2: } & \max_{\Omega, \Theta} \min_{1 \leq l \leq L, 1 \leq k \leq K_l} r_{kl}, \\
& \text{s.t. } 0 \leq x_l \leq 5.7, 0 \leq y_l \leq 8.8, 1 \leq l \leq L,
\end{aligned} \tag{3-6}$$

where  $\Omega = \{(x_l, y_l), 1 \leq l \leq L\}$ ,  $\Theta = \{\mathbf{U}_l, \mathbf{V}_l, 1 \leq l \leq L\}$ ,  $(x_l, y_l)$  is the horizontal location of cell  $l$ , and  $r_{kl}$  is the transmission rate of UE  $k$  in cell  $l$ . Notice that both optimization objectives need the computation of the transmission rate per UE. In the following, we give the expression of transmission rate for the single-cell scenario, two-cell scenario operating in the same frequency band and two-cell scenario operating in different frequency bands, respectively.

### 3.3.1. Single-cell Scenario

In the single-cell scenario, we have  $L = 1$ . The transmission rate of UE  $k$  is given by

$$r_k^S = W \log_2 \left( 1 + \frac{\frac{P}{K_l} |\mathbf{h}_{k1}^H \mathbf{U}_1 \mathbf{v}_{k1}|^2}{\frac{P}{K_l} \sum_{i=1, i \neq k}^K |\mathbf{h}_{i1}^H \mathbf{U}_1 \mathbf{v}_{i1}|^2 + \sigma_n^2} \right), \tag{3-7}$$

where  $W$  is the channel bandwidth.

### 3.3.2. Two-cell Scenario

#### 3.3.2.1. Two Cells Operating in the Same Frequency Band

In the two-cell scenario, we have  $L = 2$ . When the two cells operate in the same frequency band, the transmission rate of UE  $k$  in cell  $l$  is given by

$$r_{kl}^{T,S} = W \log_2 \left( 1 + \frac{\frac{P}{K_l} |\mathbf{h}_{kl}^H \mathbf{U}_l \mathbf{v}_{kl}|^2}{\left| \sum_{j=1}^2 \sum_{i=1}^{K_j} \sqrt{\frac{P}{K_j}} \mathbf{h}_{kj}^H \mathbf{U}_j \mathbf{v}_{ij} - \sqrt{\frac{P}{K_l}} \mathbf{h}_{kl}^H \mathbf{U}_l \mathbf{v}_{kl} \right|^2 + \sigma_n^2} \right). \tag{3-8}$$

#### 3.3.2.2. Two Cells Operating in Different Frequency Bands

When the two cells operate in different frequency bands, the transmission rate of UE  $k$  in cell  $l$  is given by

$$r_{kl}^{T,D} = \frac{W}{2} \log_2 \left( 1 + \frac{\frac{P}{K_l} |\mathbf{h}_{kl}^H \mathbf{U}_l \mathbf{v}_{kl}|^2}{\frac{P}{K_l} \sum_{i=1, i \neq k}^{K_l} |\mathbf{h}_{il}^H \mathbf{U}_l \mathbf{v}_{il}|^2 + \frac{\sigma_n^2}{2}} \right). \tag{3-9}$$

## 3.4. Joint Optimization of Small-cell Deployment and Hybrid Beamforming

In this section we solve the optimization problems in (3-5) and (3-6). We optimize the locations of small-cells using greedy search. More specifically, for the one-cell scenario, we iteratively search all the possible locations of the cell with search resolution 0.1 m, i.e., the total number of searches is  $57 \times 88$ . For each location, we optimize the hybrid beamforming according to section 3.2. Then we compute the transmission rate of each UE using (3-7) and the sum user rate/minimum user rate. Finally we obtain the best location of the cell that maximizes the sum user rate/minimum user rate.

For the two-cell scenario, we also iteratively search all the possible locations of the cells with search resolution 0.1 m and the total number of searches is  $(57 \times 88)^2$ . The difference from the single-cell scenario is that we need to consider the user association. To enhance the fairness, we assume that each cell has  $\frac{K}{2}$  UEs. For a fixed location combination, the user association strategy is introduced as follows: firstly each UE connects to the cell providing the strongest received signal; for each cell, if the number of UEs connected to it is more than  $\frac{K}{2}$ , keep the  $\frac{K}{2}$

UEs with the strongest received signals, and move other UEs to another cell. After user association, we optimize the hybrid beamforming according to section 3.2. Then we compute the transmission rate of each UE and the sum user rate/minimum user rate using (3-8)/(3-9). Finally we obtain the best location combination of the two cells that maximizes the sum user rate/minimum user rate.

### 3.5. Performance Comparison of Single-cell Scenario and Two-cell Scenario

In this section, we show the numerical results for the proposed small-cell deployment and hybrid beamforming optimization schemes. The simulation parameters are set as  $K = 12$ ,  $W = 1$  GHz,  $\sigma_n^2 = -74$  dBm,  $\alpha = 2$  and  $f = 28$  GHz. For the single-cell scenario,  $P = 23$  dBm and  $M_t = 12$ . For the two-cell scenario, for fair comparison,  $P = 20$  dBm and  $M_t = 6$ . The horizontal locations of the UEs are set as (2.5,2.6), (2.5,3), (2.5,3.4), (2.5,4.4), (2.5,4.8), (2.5,5.2), (2.9,2.6), (2.9,3), (2.9,3.4), (2.9,4.4), (2.9,4.8), (2.9,5.2) m, respectively, and the UE height is set as 0.6 m.

#### 3.5.1. Sum User Rate

For the single-cell scenario, we visualize the sum user rate in Gbps versus the cell location in Fig. 3-2. As can be seen, MMSE precoder provides the maximum sum user rate among the four digital precoders. Moreover, for all the precoders, the distributions of sum user rate are irregular due to the complex channel gain caused by the analog precoder. Generally the best locations that maximize the sum user rate are distributed near the center of the UEs. Since ZF and MMSE precoders provide much better sum user rate than the other two precoders, in the following, we will focus on the results using these two precoders.

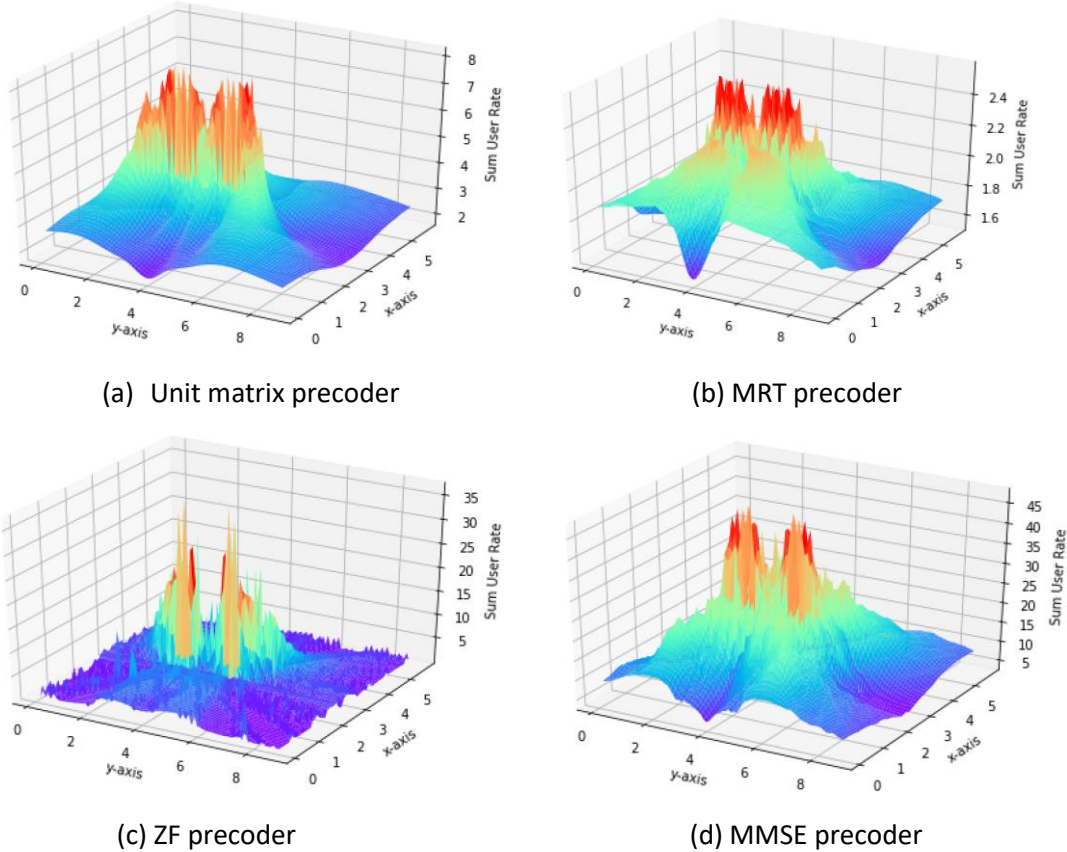


Fig. 3-2. Sum user rate versus cell location.

Table. 3-1. Maximum sum user rate

	ZF precoder	MMSE precoder
Single-cell scenario	36.74 Gbps	47.59 Gbps
Two cells operating in the same frequency band	34.03 Gbps	23.68 Gbps
Two cells operating in different frequency bands	39.48 Gbps	39.49 Gbps

In Table. 3-1, we show the maximum sum user rate achieved in the aforementioned three scenarios with ZF precoder and MMSE precoder, respectively. We can see that deploying one cell using MMSE precoder can provide the maximum sum user rate. The optimal small-cell location is (2.7, 3.1)/(2.7,4.7) m.

### 3.5.2. Minimum User Rate

Minimum user rate is an important performance metric that can be used to evaluate the fairness of UE transmission rate. In Table. 3-2, we show the maximum minimum user rate achieved in the aforementioned three scenarios with ZF precoder and MMSE precoder, respectively. We can see that deploying two cells operating at different frequency bands using ZF/MMSE precoder can provide the maximum minimum user rate. This is because operating at different frequency bands cancels the severe inter-cell interference in a small meeting room. Moreover, compared with the one-cell scenario, deploying two cells reduces the maximum cell-UE distance, which improves the minimum user rate. The optimal combinations of the two small-cell locations are (2.7, 3.3), (2.7,5.1)/ 2.7, 3.3), (2.7,4.5)/(2.7, 2.7), (2.7,5.1)/ (2.7, 2.7), (2.7,4.5) m.

Table. 3-2. Maximum minimum user rate

	ZF precoder	MMSE precoder
Single-cell scenario	0.17 Gbps	1 Gbps
Two cells operating in the same frequency band	0.8 Gbps	0.91 Gbps
Two cells operating in different frequency bands	3.01 Gbps	3.01 Gbps

### 3.6. Recommendation

We have jointly optimized the deployment of small-cells and hybrid beamforming to maximize the sum user rate/minimum user rate in a meeting room. For fixed small-cell locations, we have obtained the optimal precoder by maximizing the desired signal received by each UE assuming that the digital precoder is a unit matrix. We have adopted four typical digital precoders: unit matrix, MRT, ZF and MMSE. We have obtained the optimal locations of small-cells that maximize the sum user rate/minimum user rate through greedy search. We have compared the network performance in terms of sum user rate and minimum user rate in the single-cell scenario and two-cell scenario. The numerical results show that deploying one cell using MMSE precoder provides the maximum sum user rate and deploying two cells operating at different frequency bands using ZF/MMSE precoder provides the maximum minimum user rate. Notice that these conclusions may be different in an indoor environment with larger space.

## 4. Optimising the Wireless Friendliness of Indoor Building Materials

Internet of things (IoT) connects numerous heterogeneous devices, and provides infrastructures for smart buildings, smart grids, and smart cities. With the roll-out of 5G systems and the opening horizon of 6G systems, cellular networks will provide economical, flexible and reliable wireless connectivity for IoT devices, e.g., by leveraging 5G massive machine type communication (mMTC) and 6G massive broad bandwidth machine type (mBBMT) technologies.

It is predicted that 80-96% of wireless data traffic will be consumed indoors in the future [11]. As a result, indoor wireless traffic required by IoT is growing at an unprecedented rate. Notably, physical obstacles like walls would affect the indoor propagation of electromagnetic (EM) waves. Therefore, indoor wireless performance should be one of the indispensable prerequisites when designing buildings [12].

To meet the high data demand and address the capacity crunch in-building, indoor small base stations (BSs) are usually equipped with large-scale antenna arrays, e.g., consisting of hundreds of antennas, facilitated by multiple-input multiple-output (MIMO) technology to achieve spatial multiplexing/diversity gains. In order to guarantee a low spatial correlation, the space intervals among antenna elements of the MIMO antenna array have to be larger than half wavelength [13], which therefore will increase the physical dimension of the indoor small BSs and generate negative weight and visual consequence on a room. Especially in industrial environment, deploying BSs in the workspace may increase the risk of accidents.

To avoid any possible negative impact on the functionality and appearance of a room, a desirable indoor BS deployment is to integrate MIMO antenna arrays with interior walls [14,15], which however will result in non-negligible coupling between MIMO antenna arrays and building materials [16]. Specifically, when an EM wave impinges on a wall surface, the intensity of the wall reflected wave can be measured by the reflection coefficient, which depends on the EM and physical properties of the wall material, i.e., its relative permittivity and thickness [17]. The wall reflected EM waves would be superposed with other EM waves, which may jointly influence the indoor wireless performance. Hence, enhancing indoor wireless performance requires a rational selection and/or design of building materials. In this work, we define the wireless friendliness as a new performance metric of a building material, which is characterised by its relative permittivity and thickness. A building material with desirable wireless friendliness would be beneficial to the performance of indoor wireless networks.

The work presented in this section was published [18].

### 4.1 System Model

In this subsection, we introduce a novel system model for indoor LOS MIMO communications that incorporates the wall reflection (WR) path and the EM and physical properties of the building material.

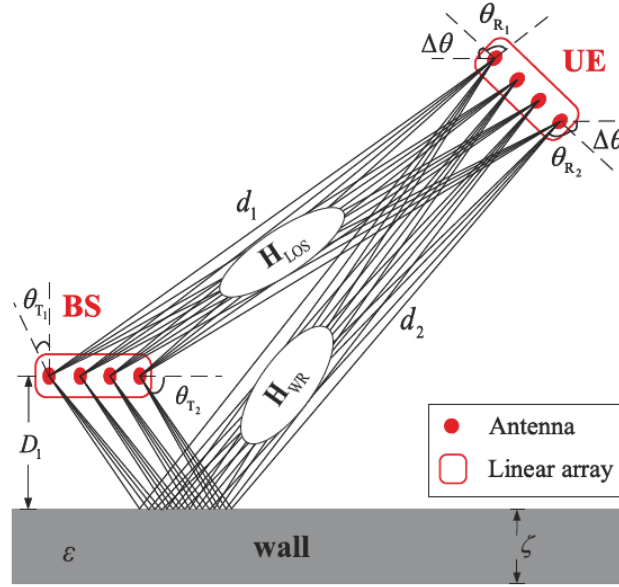


Fig. 4-1 The LOS path and the WR path between indoor BS and UE.

We consider indoor LOS MIMO downlink transmissions, as shown in Fig. 4-1. In the considered room, one BS is deployed close to one of the walls and one UE could be arbitrarily positioned. Since the strength of a WR path from a wall other than the wall that is closest to the BS will be dominated by the distance-dependent path loss, the reflected paths from the other walls would be much weaker than the WR path from the wall closest to the BS. Hence, the considered wall refers to the wall closest to the BS hereafter, and the WR path refers to the wall reflected path from the considered wall. The BS is deployed in parallel with the considered wall with a small distance of  $D_1$  from the wall. The BS and a typical UE are equipped with  $N_T$  and  $N_R$  omnidirectional antennas, respectively, both in linear arrays with inter-antenna spacing  $D$ . The complex frequency-flat linear channel from the BS to the typical UE is constructed as

$$\mathbf{y} = \mathbf{H}\mathbf{x} + \mathbf{n}, \quad (4-1)$$

where  $\mathbf{x} \in \mathbb{C}^{N_T \times 1}$ ,  $\mathbf{y} \in \mathbb{C}^{N_R \times 1}$  denote the transmitted signal and the received signal, respectively,  $\mathbf{n}$  denotes the additive white Gaussian noise, and  $\mathbf{H}$  is a  $N_R \times N_T$  channel matrix, subject to  $E[\text{Tr}\{\mathbf{H}\mathbf{H}^H\}] = N_R N_T$ , where  $E(\cdot)$  and  $\text{Tr}\{\cdot\}$  denote the expectation and the trace of a matrix, respectively.

Other than the LOS path, the WR path is taken into account to capture the impact of building materials on the indoor wireless propagation channel.

For a certain position in the room, the LOS path and the WR path are deterministically modelled by Friis' formula as  $N_R \times N_T$  matrix  $\mathbf{H}_{\text{LOS}}$  and  $\mathbf{H}_{\text{WR}}$ , respectively, whose elements are given as

$$[\mathbf{H}_{\text{LOS}}]_{n_R, n_T} = \frac{\mu}{4\pi d_1} e^{-j \frac{2\pi}{\mu} \left( d_1 + D \left( \left( n_R - \frac{N_R - 1}{2} \right) \cos \theta_{R1} + \left( n_T - \frac{N_T - 1}{2} \right) \cos \theta_{T1} \right) \right)} \quad (4-2)$$

$$[\mathbf{H}_{\text{WR}}]_{n_R, n_T} = \frac{\mu \Gamma}{4\pi d_2} e^{-j \frac{2\pi}{\mu} \left( d_2 + D \left( \left( n_R - \frac{N_R - 1}{2} \right) \cos \theta_{R2} + \left( n_T - \frac{N_T - 1}{2} \right) \cos \theta_{T2} \right) \right)} \quad (4-3)$$



in which  $n_T \in \{0, 1, \dots, N_T - 1\}$  and  $n_R \in \{0, 1, \dots, N_R - 1\}$  are the indices of transmit and receive antenna elements,  $\mu$  denotes the wavelength of EM waves in the air,  $d_1$  and  $d_2$  denote the length of the LOS path and the WR path, respectively,  $\theta_{T_1}$  and  $\theta_{T_2}$  denote the approximated angle of departure (AoD) of the LOS path and the WR path at the BS array, respectively, while  $\theta_{R_1}$  and  $\theta_{R_2}$  denote the approximated angle of arrival (AoA) of the LOS path and the WR path at the UE array, respectively, and  $\Gamma$  represents the equivalent reflection coefficient of the WR path. Along the WR path, multiple internal reflections are considered when the EM wave interacts with the building material. Considering the building material as a single-layer dielectric reflector,  $\Gamma$  represents the equivalent reflection coefficient of the WR path.

Along the WR path, multiple internal reflections are considered when the EM wave interacts with the building material. Using plane wave far-field approximation, the incident angles of different order reflections are all approximated by  $\alpha$ . When the building material is assumed to be a single-layer homogenous dielectric reflector with relative permittivity  $\varepsilon$  and thickness  $\zeta$ , the equivalent reflection coefficient of the WR path is represented as [17]

$$\Gamma = \frac{1 - \exp(-j2\delta)}{1 - (\Gamma')^2 \exp(-j2\delta)} \Gamma' \quad (4-4)$$

where

$$\delta = \frac{2\pi\zeta}{\mu} \sqrt{\varepsilon - \sin^2 \alpha} \quad (4-5)$$

and the first-order reflection coefficient  $\Gamma'$  represents the transverse electric (TE) polarisation  $\Gamma_{TE}$  or the transverse magnetic (TM) polarisation  $\Gamma_{TM}$  of the incident electric field, respectively, which are given by:

$$\Gamma_{TE} = \frac{\cos \alpha - \sqrt{\varepsilon - \sin^2 \alpha}}{\cos \alpha + \sqrt{\varepsilon - \sin^2 \alpha}}, \quad (4-6)$$

$$\Gamma_{TM} = \frac{\cos \alpha - \sqrt{(\varepsilon - \sin^2 \alpha) / \varepsilon^2}}{\cos \alpha + \sqrt{(\varepsilon - \sin^2 \alpha) / \varepsilon^2}}. \quad (4-7)$$

For simplicity,  $\mathbf{H}_{LOS}$  and  $\mathbf{H}_{WR}$  are merged as one matrix  $\mathbf{H}_1$ , which can be decomposed as

$$\mathbf{H}_1 = A_1 \mathbf{h}_{\beta_1}^H \mathbf{h}_{\alpha_1} + A_2 \mathbf{h}_{\beta_2}^H \mathbf{h}_{\alpha_2}, \quad (4-8)$$

$$A_1 = \frac{\mu \sqrt{N_T N_R}}{4\pi d_1} e^{-j2\pi \frac{d_1}{\mu}},$$

$$A_2 = \frac{\mu \Gamma \sqrt{N_T N_R}}{4\pi d_2} e^{-j2\pi \frac{d_2}{\mu}},$$

$$\alpha_i = 2\pi D \cos \theta_{T_i} / \mu,$$

$$\beta_i = 2\pi D \cos(\theta_{R_i} + \Delta\theta) / \mu,$$



$$\mathbf{h}_{\alpha_l} = \left( \frac{e^{-j\left(\frac{N_T-1}{2}\right)\alpha_l}}{\sqrt{N_T}}, \frac{e^{-j\left(1-\frac{N_T-1}{2}\right)\alpha_l}}{\sqrt{N_T}}, \dots, \frac{e^{-j\left(\frac{N_T-1}{2}\right)\alpha_l}}{\sqrt{N_T}} \right),$$

$$\mathbf{h}_{\beta_l} = \left( \frac{e^{j\left(\frac{N_R-1}{2}\right)\beta_l}}{\sqrt{N_R}}, \frac{e^{j\left(1-\frac{N_R-1}{2}\right)\beta_l}}{\sqrt{N_R}}, \dots, \frac{e^{j\left(\frac{N_R-1}{2}\right)\beta_l}}{\sqrt{N_R}} \right),$$

where  $l \in \{1, 2\}$ .

Based on distance-dependant Rician fading model and the multipath (MP) effect, our channel matrix  $\mathbf{H}$  consists of three components including the LOS part, the WR part, and the MP part, which can be presented as

$$\mathbf{H} = \sqrt{\frac{\bar{K}}{1+\bar{K}}} \bar{\mathbf{H}} + \sqrt{\frac{1}{1+\bar{K}}} \mathbf{H}_{\text{MP}}, \quad (4-9)$$

where the deterministic matrix  $\bar{\mathbf{H}}$ , including the LOS part and the WR part, is expressed as

$$\bar{\mathbf{H}} = \frac{\mathbf{H}_1}{\|\mathbf{H}_1\|} \sqrt{N_R N_T}, \quad (4-10)$$

subject to  $E[\text{Tr}\{\mathbf{H}\mathbf{H}^\dagger\}] = N_R N_T$ , with  $\|\cdot\|$  denoting the F-norm. The MP components are assumed to be independent and identically distributed zero mean and unit variance complex Gaussian random variables arranged in the  $N_R \times N_T$  matrix  $\mathbf{H}_{\text{MP}}$ .

$\bar{K}$  is the power ratio between the deterministic part  $\bar{\mathbf{H}}$  and the random part  $\mathbf{H}_{\text{MP}}$ , which can be obtained through

$$\bar{K} = \bar{K}_0 S, \quad (4-11)$$

where  $\bar{K}_0$  is the distance-dependant Rician factor as a function of  $d_1$  defining the power ratio between the LOS part and the MP part [19], given by

$$\bar{K}_0 = 8.7 + 0.051d_1 \text{ (dB)}, \quad (4-12)$$

$$S = \frac{\|\mathbf{H}_1\|^2}{\|A_1 \mathbf{h}_{\beta_1}^H \mathbf{h}_{\alpha_1}\|^2} = \frac{d_1^2}{d_2^2} |\Gamma|^2 + \frac{2\bar{S}d_1}{N_T N_R d_2} + 1, \quad (4-13)$$

$$\bar{S} = \text{Re} \left( \Gamma e^{-j2\pi \frac{d_2 - d_1}{\mu}} \right) \frac{\sin\left(\frac{N_T}{2}(\alpha_2 - \alpha_1)\right)}{\sin\left(\frac{1}{2}(\alpha_2 - \alpha_1)\right)} \frac{\sin\left(\frac{N_R}{2}(\beta_2 - \beta_1)\right)}{\sin\left(\frac{1}{2}(\beta_2 - \beta_1)\right)}, \quad (4-14)$$

where  $\text{Re}(\cdot)$  denotes the real part of a complex value.

## 4.2 Channel Capacity

In this section, for an arbitrary position in the room, we derive the two non-zero squared singular values of  $\mathbf{H}_1$ , the MPDF of an unordered squared singular value, and the ergodic capacity of an indoor LOS MIMO channel  $\mathbf{H}$  in closed forms.

### 4.2.1 The distribution of the squared singular value of channel

For notational convenience, we define  $m = \min\{N_R, N_T\}$  and  $n = \max\{N_R, N_T\}$ .

Lemma 1: Suppose  $\varphi_1, \varphi_2, \dots, \varphi_m$  are the  $m$  squared singular values of  $\mathbf{H}_1$ , where  $\varphi_1, \varphi_2, \dots, \varphi_{m-2} = 0$  and  $\varphi_{m-1}, \varphi_m > 0$ . The two non-zero squared singular values of  $\mathbf{H}_1$  are computed in closed-form as

$$\varphi_{m-1} = \frac{\|\mathbf{X}\|^2 - \sqrt{\|\mathbf{X}\|^4 - 4|\det(\mathbf{X})|^2}}{2}, \quad (4-15)$$

$$\varphi_m = \frac{\|\mathbf{X}\|^2 + \sqrt{\|\mathbf{X}\|^4 - 4|\det(\mathbf{X})|^2}}{2}, \quad (4-16)$$

$$\mathbf{X} = \begin{bmatrix} A_1 + A_2 \Delta \beta \Delta \alpha & A_2 \Delta \beta \|\mathbf{h}_{\alpha_s}\| \\ A_2 \Delta \alpha \|\mathbf{h}_{\beta_s}\| & A_2 \|\mathbf{h}_{\alpha_s}\| \|\mathbf{h}_{\beta_s}\| \end{bmatrix},$$

$$\mathbf{h}_{\beta_s}^H = \mathbf{h}_{\beta_2}^H - \Delta \beta \mathbf{h}_{\beta_1}^H,$$

$$\mathbf{h}_{\alpha_s} = \mathbf{h}_{\alpha_2} - \Delta \alpha \mathbf{h}_{\alpha_1},$$

$$\Delta \beta = \langle \mathbf{h}_{\beta_2}^H, \mathbf{h}_{\beta_1}^H \rangle = \frac{1}{N_R} \sum_{q=-(N_R-1)/2}^{(N_R-1)/2} \exp(jq(\beta_1 - \beta_2)) = \frac{\sin(\pi N_R D (\cos \theta_{R_1} - \cos \theta_{R_2}) / \mu)}{N_R \sin(\pi D (\cos \theta_{R_1} - \cos \theta_{R_2}) / \mu)}$$

$$\Delta \alpha = \langle \mathbf{h}_{\alpha_2}, \mathbf{h}_{\alpha_1} \rangle = \frac{1}{N_T} \sum_{q=-(N_T-1)/2}^{(N_T-1)/2} \exp(jq(\alpha_1 - \alpha_2)) = \frac{\sin(\pi N_T D (\cos \theta_{T_1} - \cos \theta_{T_2}) / \mu)}{N_T \sin(\pi D (\cos \theta_{T_1} - \cos \theta_{T_2}) / \mu)}$$

*Proof:*

Since two deterministic components including the LOS path and the WR path are considered in our model, it is obvious that  $\mathbf{H}_1$  has two non-zero singular values. The singular value decomposition of deterministic part  $\mathbf{H}_1$  can be given as

$$\mathbf{H}_1 = \mathbf{B}^H \mathbf{X} \mathbf{A}, \quad (4-17)$$

where

$$\mathbf{B} = \begin{pmatrix} \mathbf{h}_{\beta_1} & \mathbf{h}_{\beta_s} / \|\mathbf{h}_{\beta_s}\| \end{pmatrix}^T,$$

$$\mathbf{A} = \begin{pmatrix} \mathbf{h}_{\alpha_1} & \mathbf{h}_{\alpha_s} / \|\mathbf{h}_{\alpha_s}\| \end{pmatrix}^T,$$

$$\mathbf{X} = \begin{pmatrix} 1 & \Delta\beta \\ 0 & \|\mathbf{h}_{\beta_s}\| \end{pmatrix} \begin{pmatrix} A_1 & 0 \\ 0 & A_2 \end{pmatrix} \begin{pmatrix} 1 & 0 \\ \Delta\alpha & \|\mathbf{h}_{\alpha_s}\| \end{pmatrix}.$$

Following Gram-Schmidt process,  $\mathbf{h}_{\alpha_1}$  and  $\mathbf{h}_{\beta_1}^H$  are orthonormalized with  $\mathbf{h}_{\alpha_s} / \|\mathbf{h}_{\alpha_s}\|$  and  $\mathbf{h}_{\beta_s}^H / \|\mathbf{h}_{\beta_s}^H\|$ , respectively, which means that  $\mathbf{B}^H \mathbf{B} = \mathbf{I}$  and  $\mathbf{A}^H \mathbf{A} = \mathbf{I}$ .

Matrix  $\mathbf{X}$  can be simplified as a  $2 \times 2$  matrix, with the four elements given in Lemma 1. Assuming  $\mathbf{X}$  could be decomposed as

$$\mathbf{X} = \mathbf{P}^H \begin{pmatrix} \sqrt{\varphi_{m-1}} & 0 \\ 0 & \sqrt{\varphi_m} \end{pmatrix} \mathbf{Q}, \quad (4-18)$$

where  $\mathbf{P}^H \mathbf{P} = \mathbf{I}$  and  $\mathbf{Q}^H \mathbf{Q} = \mathbf{I}$ , then  $\varphi_{m-1}$  and  $\varphi_m$  are two squared singular values of matrix  $\mathbf{X}$ .

Hence we obtain

$$\mathbf{H}_1 = (\mathbf{P}\mathbf{B})^H \begin{pmatrix} \sqrt{\varphi_{m-1}} & 0 \\ 0 & \sqrt{\varphi_m} \end{pmatrix} \mathbf{Q}\mathbf{A}. \quad (4-19)$$

Here it is interesting to find that  $\varphi_{m-1}$  and  $\varphi_m$  are the two squared singular values of  $\mathbf{H}_1$  as well, since  $(\mathbf{P}\mathbf{B})^H \mathbf{P}\mathbf{B} = \mathbf{I}$  and  $(\mathbf{Q}\mathbf{A})^H \mathbf{Q}\mathbf{A} = \mathbf{I}$ .

Therefore, the two non-zero squared singular values of  $\mathbf{H}_1$ , i.e.  $\varphi_{m-1}$  and  $\varphi_m$ , can be easily obtained by conducting singular value decomposition to low dimensional matrix  $\mathbf{X}$ , as given in (4-15) and (4-16) of Lemma 1.

**Theorem 1:** The MPDF of an unordered squared singular value  $\lambda$  of  $\mathbf{H}$  is computed as follows

$$f(\lambda) = \frac{e^{-\phi_m - \phi_{m-1} - (\bar{K}+1)\lambda}}{m((n-m)!)^2 \lambda} \sum_{j=1}^m \frac{((\bar{K}+1)\lambda)^{n-m+j}}{(\phi_m \phi_{m-1})^{m-2} (\phi_m - \phi_{m-1}) \prod_{l=0}^{m-3} l! (n-m+l)!} \\ \left( \sum_{i=1}^{m-2} D_{i,j} ((\bar{K}+1)\lambda)^{i-1} + D_{m-1,j0} F_1(n-m+1, (\bar{K}+1)\phi_{m-1}\lambda) + D_{m,j0} F_1(n-m+1, (\bar{K}+1)\phi_m\lambda) \right) \quad (4-20)$$

where the two non-zero squared singular values of  $\sqrt{\bar{K}}\bar{\mathbf{H}}$  are given by

$$\phi_{m-1} = \frac{\bar{K}N_R N_T \varphi_{m-1}}{\|\mathbf{H}_1\|^2} = \frac{\bar{K}_0 N_R N_T \varphi_{m-1}}{\|A_1\|^2}, \quad (4-21)$$

$$\phi_m = \frac{\bar{K}N_R N_T \varphi_m}{\|\mathbf{H}_1\|^2} = \frac{\bar{K}_0 N_R N_T \varphi_m}{\|A_1\|^2}, \quad (4-22)$$

And  $D_{i,j}$  is the  $(i, j)$  co-factor of the  $m \times m$  matrix  $\mathbf{Z}$  whose  $(l, k)$ th entry is given by

$$(\mathbf{Z})_{l,k} = \begin{cases} (n-m+k+l-2)!, & 1 \leq l \leq m-2, \\ \frac{{}_1F_1(n-m+l, n-m+1, \phi_k)}{((n-m+l-1)!)^{-1}}, & \text{otherwise.} \end{cases} \quad (4-23)$$

The hypergeometric function  ${}_0F_1(w, z^2)$  is defined in the series form by

$${}_0F_1(w, z^2) = \sum_{s=0}^{\infty} \frac{(z)^{2s}}{s! [w]_s}, \quad (4-24)$$

and the hypergeometric function  ${}_1F_1(e, o, g)$  is given by

$${}_1F_1(e, o, g) = \sum_{s=0}^{\infty} \frac{[e]_s g^s}{[o]_s s!}, \quad (4-25)$$

$$\text{where } [r]_t = \frac{(r+t-1)!}{(r-1)!}.$$

Proof: Given the channel model in (4-9)-(4-14), the channel matrix  $\mathbf{H}$  is an  $N_R$ -by- $N_T$  non-central Wishart matrix with mean  $\sqrt{\frac{\bar{K}}{1+\bar{K}}} \bar{\mathbf{H}}$ . Hence, the MPDF of an arbitrary squared value of  $\mathbf{H}$  can be found in [20, (3)], which is derived by the squared singular values of  $\sqrt{\bar{K}} \bar{\mathbf{H}}$ .

Since  $\mathbf{H}_1$  has only two non-zero squared singular values given in Lemma 1 and the relationship between  $\mathbf{H}_1$  and  $\bar{\mathbf{H}}$  is given in (4-10), the two non-zero squared singular values of  $\sqrt{\bar{K}} \bar{\mathbf{H}}$  are given in (4-21) and (4-22), respectively, based on (4-15) and (4-16).

Meanwhile, using [20, Lemma 2], we get

$$\lim_{\tau \rightarrow 0} \frac{{}_0F_1(n-m+1, (\bar{K}+1)(\phi_i + \tau_i)\lambda) C_{i,j}(\phi_i + \tau_i)}{\prod_{k < l}^m ((\phi_l + \tau_l) - (\phi_k + \tau_k))} = \frac{f_i(\lambda) D_{i,j}(\phi_i + \tau_i)}{\prod_{l=1}^{m-2} (l-1)! \prod_{l=m-1}^m \phi_l^{m-2} (\phi_m - \phi_{m-1})}, \quad (4-26)$$

where  $\boldsymbol{\tau} = \{\tau_1, \tau_2, \dots, \tau_m\}$  is an  $m$ -dimensional vector whose elements are distinct,

$$f_i(\lambda) = \begin{cases} \lambda^{i-1} [n-m+1]_{i-1}^{-1}, & 1 \leq i \leq m-2, \\ {}_0F_1(n-m+1, (\bar{K}+1)\phi_i\lambda), & \text{otherwise,} \end{cases} \quad (4-27)$$

$D_{i,j}$  is given in (4-23) and  $C_{i,j}$  in [20, (3)] is the  $(i, j)$ -co-factor of the  $m \times m$  matrix  $\mathbf{A}$  whose  $(i, j)$  th entry is  $\mathbf{A}_{i,j} = (n-m+j-1)! {}_0F_1(n-m+j, n-m+1, \phi_i)$ . Since  $\mathbf{H}$  has only two non-zero squared values, its MPDF can be derived as (4-20) by substituting (4-26) and (4-27) into [20, (3)].

#### 4.2.2 Closed-form ergodic capacity

Theorem 2: The ergodic capacity at a typical position is given by

$$C(\rho) = \kappa \sum_{j=1}^m \left( \sum_{i=1}^{m-2} \frac{(g-1)!}{(D_{i,j})^{-1}} \sum_{k=1}^g E_{g-k+1} \left( \frac{\bar{K}+1}{\rho / N_T} \right) + \sum_{p=0}^{\infty} \frac{(D_{m-1,j} \phi_{m-1}^p + D_{m,j} \phi_m^p)}{p!(n-m+p)!((\tau-1)!(n-m)!)} \sum_{k=1}^{\tau} E_{\tau-k+1} \left( \frac{\bar{K}+1}{\rho / N_T} \right) \right) \quad (4-28)$$

where the average signal-to-noise-ratio (SNR) at each receiver branch is given by

$$\rho = \frac{\bar{K} \|\mathbf{H}_1\|^2 \rho_T}{(\bar{K}+1) N_R N_T}, \quad (4-29)$$

In which  $\rho_T = E(\|\mathbf{x}\|^2) / E(\|\mathbf{n}\|^2)$  refers to the SNR at transmitter side,

$$\kappa = \frac{\exp \left( \frac{\bar{K}+1}{\rho / N_T} - \phi_m - \phi_{m-1} \right)}{\ln 2 ((n-m)!)^{m-1} (\phi_m \phi_{m-1})^{m-2} (\phi_m - \phi_{m-1}) \prod_{l=0}^{m-3} l!}, \quad (4-30)$$

$$g = n - m + j + i - 1, \quad \tau = n - m + j + p, \quad \text{and} \quad E_Q(x) = \int_1^{\infty} e^{-xt} t^{-Q} dt.$$

Proof: The ergodic capacity can be derived by taking the expectation with respect to  $\lambda$  as follows [21]

$$C(\rho) = m E \left[ \log_2 \left( 1 + \frac{\rho}{N_T} \lambda \right) \right] = m \int_0^{\infty} \log_2 \left( 1 + \frac{\rho}{N_T} \lambda \right) f(\lambda) d\lambda, \quad (4-31)$$

where  $f(\lambda)$  is given in (4-20). The integral over  $\lambda$  in (4-31) is computed by the series expansion of  ${}_0F_1(n-m+1, (\bar{K}+1)\phi_i\lambda)$  in (4-24) and

$$\int_0^{\infty} \ln(1 + \varpi \lambda) \lambda^{\eta-1} e^{-\gamma \lambda} d\lambda = \frac{(\eta-1)!}{e^{\frac{\gamma}{\varpi}} \gamma^{\eta}} \sum_{l=1}^{\eta} E_{\eta-l+1} \left( \frac{\gamma}{\varpi} \right) \quad (4-32)$$

in [22, Appendix A]. Thus, the ergodic capacity at a typical UE position is given in (4-28).

#### 4.3 Wireless Friendliness Evaluation Scheme

In this subsection, we investigate how friendly a wall made of a single-layer material is to indoor LOS MIMO transmissions. Aiming to quantify the wireless friendliness of a building material, a reasonable indicator is the expectation of capacity. However, the value of  $E(C)$  cannot be calculated straightforwardly. An alternative solution is to average the capacity values over dense sample points inside the room, since the limit of the mean capacity values over sample points equals  $E(C)$  as the sampling density approaches infinity.

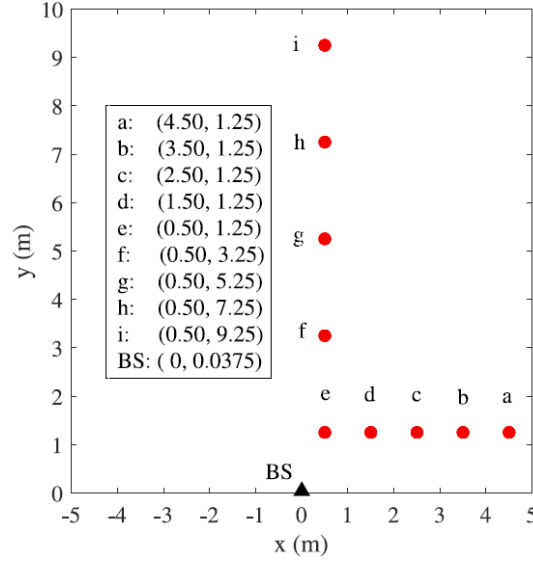


Fig. 4-2 Cartesian coordinates for a room, e.g.,  $W_0 = L_0 = 10$  m, where the BS is close to the considered wall and there is an L-shaped route inside.

Building a two-dimensional Cartesian coordinate system inside a  $W_0 \times L_0$  as shown in Fig. 4-2, we take  $X \times Y$  sample points spatially evenly distributed throughout the room. The origin is set at the middle point along the  $\$L\$$  side and the considered room is defined within the area of  $x \in [-L_0/2, L_0/2]$  and  $y \in [0, W_0]$ . For a UE at the location  $(x_i, y_j)$  where  $i \in \{1, 2, \dots, X\}$  and  $j \in \{1, 2, \dots, Y\}$ , its downlink ergodic capacity can be computed by (4-28)-(4-30) and denoted as  $C(x_i, y_j)$  in bit/s/Hz. The capacity spatially averaged over all sample points, used as an evaluation indicator for measuring the wireless friendliness of a building material, is given by

$$C_{\text{avg}} = \frac{1}{XY} \sum_{i=1}^X \sum_{j=1}^Y C(x_i, y_j). \quad (4-33)$$

According to [17], a simple expression of relative permittivity  $\varepsilon$  is given by  $\varepsilon = \varepsilon_0 - j\varepsilon_1$ , where the real part and the imaginary part can be expressed as a function of frequency  $f$ , i.e.,  $\varepsilon_0 = uf^v$  and  $\varepsilon_1 = 17.98\sigma/f$ , where  $\sigma = rf^t$  is the conductivity of the building material, and constants  $u$ ,  $v$ ,  $r$  and  $t$  are compiled in [17, Table 3]. In the following, we focus on the permittivity and thickness of the building material.

**Permittivity:** The permittivity in this paper refers to the real part of relative permittivity  $\varepsilon_0$ . The imaginary part is assumed to be a constant. Note that both  $\varepsilon$  and  $\varepsilon_0$  are unitless.

**Thickness:** Since the building material in this paper is assumed to be a homogenous dielectric reflector, the building material's thickness of  $\zeta$  equals to that of the wall.

The scheme for evaluating the wireless friendliness of a building material is given in Algorithm 1. The permittivity  $\varepsilon_0$  and the thickness  $\zeta$  of a wall material are the inputs, and the output  $C_{\text{avg}}$  is computed following (4-33) as an indicator of its wireless friendliness. A higher  $C_{\text{avg}}$  indicates

that a wall made of this kind of material would be more friendly to indoor LOS MIMO communications.

---

**Algorithm 1:** Wireless Friendliness Evaluation Scheme for a Building Material

---

**Input:**  $\varepsilon_0, \zeta, K, \mu, W, L, X, Y, N_T, N_R, D, D_1, \rho_T$

**Output:**  $C_{\text{avg}}$

```

1 Calculate the step in x axis:  $\Delta_x = \frac{W}{X}$ ;
2 Calculate the step in y axis:  $\Delta_y = \frac{L-D_1}{Y-1}$ ;
3 Determine the coordinates  $(x, y)$  of all sample points :
    $x = -W/2 + (\Delta_x/2) : \Delta_x : W/2 - (\Delta_x/2)$ ;
    $y = D_1 : \Delta_y : L$ ;
4 Determine the BS position located at  $(0, D_1)$ ;
5 for  $i = 1; i \leq X$  do
6   for  $j = 1; j \leq Y$  do
7     Determine the UE location  $(x_i, y_j)$ ;
8     Calculate  $d_1, d_2, \theta_{T1}, \theta_{T2}, \theta_{R1}$  and  $\theta_{R2}, \alpha$ ;
9     Calculate  $\Gamma$  with (4)-(7);
10    Construct  $\mathbf{H}$  with (8)-(13);
11    Derive  $C(x_i, y_j)$  with (26)-(28);
12  end for
13 Calculate  $C_{\text{avg}}$  with (31);
14 return  $C_{\text{avg}}$ ;

```

---

#### 4.4 Numerical Results

In this section, we present and analyse the numerical results for both omnidirectional and directional BS antenna arrays to present a comprehensive understanding of the impact of building materials as reflectors on indoor LOS MIMO communications.

The parameters used in the simulations are given in Table 4-1. The incident wave is assumed to be TE polarised. The transmission power of the BS is assumed to be equally allocated to every transmit antenna element. The BS is deployed at point  $(0, D_1)$  and its antenna array is deployed parallel to the considered wall. In the Monte Carlo simulations, the ergodic capacity at point  $(x_i, y_j)$  is computed by

$$C_{\text{sim}}(x_i, y_j) = \mathbb{E} \left[ \log_2 \det \left( \mathbf{I} + \frac{\rho}{N_T} \mathbf{H} \mathbf{H}^H \right) \right]. \quad (4-34)$$

Table 4-1 Main simulation assumptions

Parameter name	Parameter value
Frequency $f$ (GHz)	6
Room width $W$ (m)	10
Room length $L$ (m)	10
Inter-antenna spacing $D = \mu/2$ (m)	0.025
The distance from BS to wall $D_1$ (m)	0.0375
Number of BS antennas $N_T$	4
Number of UE antennas $N_R$	4
Samples along room $x$ axis $X$	100
Samples along room $y$ axis $Y$	100

#### 4.4.1 The ergodic capacity for a specific sample point

In this subsection, we take three points, i.e. (0.3, 0.25), (4.5, 8.0) and (-2.5, 0.55), as examples to verify the correctness of analytical expression of (4.20)-(4.22) and (4.28)-(4.30). The Rician factor  $\overline{K}_0$  of the three points is computed by (4.12) accordingly.

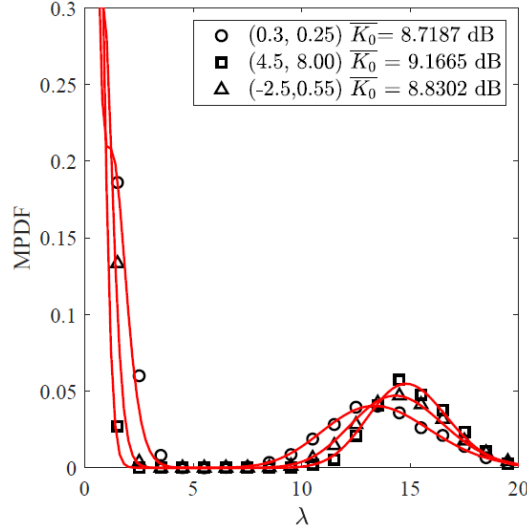


Fig. 4-3 The MPDF of an unordered squared singular value at the three points, for  $\zeta = 0.2$ ,  $\varepsilon = 5.31 - j0.5861f^{-0.1905}$ . Markers represent simulation values while lines represent analytical values.

Fig. 4-3 depicts the MPDF of an unordered squared singular value of the LOS MIMO channel. It is found that the MPDF becomes more concentrated as  $\overline{K}_0$  is reduced, which reveals that the squared singular values of matrix  $\mathbf{H}$  are more evenly distributed and thus results in a larger ergodic capacity.

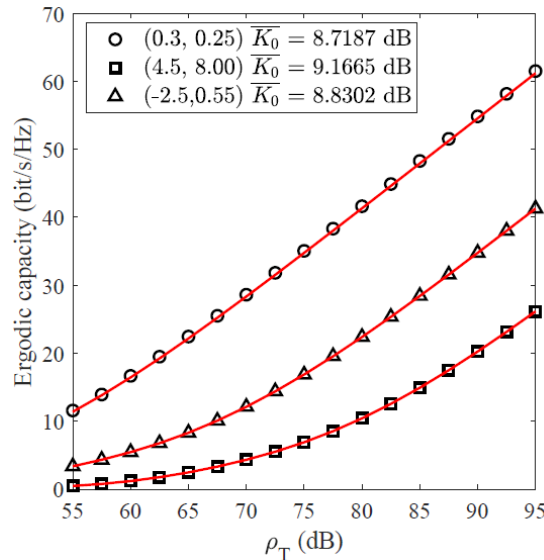


Fig. 4-4 Relationship between ergodic capacity and transmit SNR at three points, for  $\zeta = 0.2$ ,  $\varepsilon = 5.31 - j0.5861f^{-0.1905}$ . Markers represent simulation values while lines represent analytical values.



Fig. 4-4 shows the ergodic capacity versus the transmit SNR. The ergodic capacity increases when the transmit SNR increases. Meanwhile, a larger  $\overline{K}_0$  leads to a lower ergodic capacity under the same transmit SNR due to the less concentrated MPDF of an unordered squared singular value of channel matrix  $\mathbf{H}$ .

#### 4.4.2 The ergodic capacity distribution in a square room

To verify the accuracy of the evaluation indicator  $C_{\text{avg}}$  in (4.28) and the usefulness of Algorithm 1, the ergodic capacity at different positions is studied in this subsection.

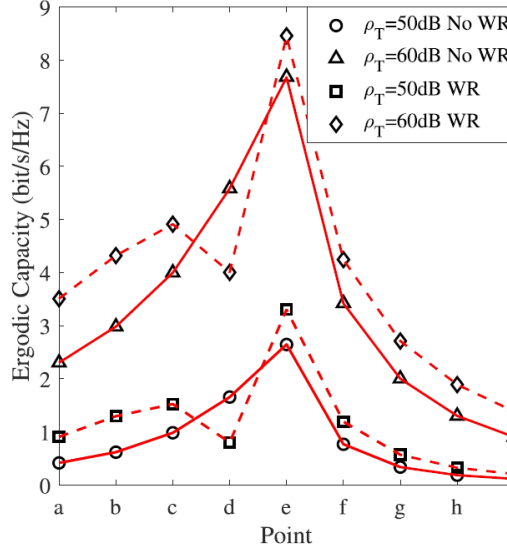


Fig. 4-5 Ergodic capacity at the points for L-shaped route, for  $\zeta = 0.2$ ,  $\varepsilon = 5.31 - j0.5861f^{-0.1905}$ . Markers represent simulation values while both the solid and dash lines represent analytical values.

We design a L-shaped route that includes some typical UE positions in the square room, as shown in Fig. 4-2. The ergodic capacities from point a to j along this route, in the presence or absence of WR path, are shown in Fig. 4-5. The dash lines illustrate the results taking into account the WR path. From point a to e, we observe an increase in capacity as the UE is approaching the BS except for point d, where the slump in ergodic capacity is due to the power cancellation caused by the destructive combination of the LOS path and the WR path. When the UE moves from point e to i, the capacity declines. This is different from the ergodic capacity under the Rician fading model without considering the WR path that would monotonically decrease with an increasing UE-BS distance, as shown by the solid lines in Fig. 4-5.

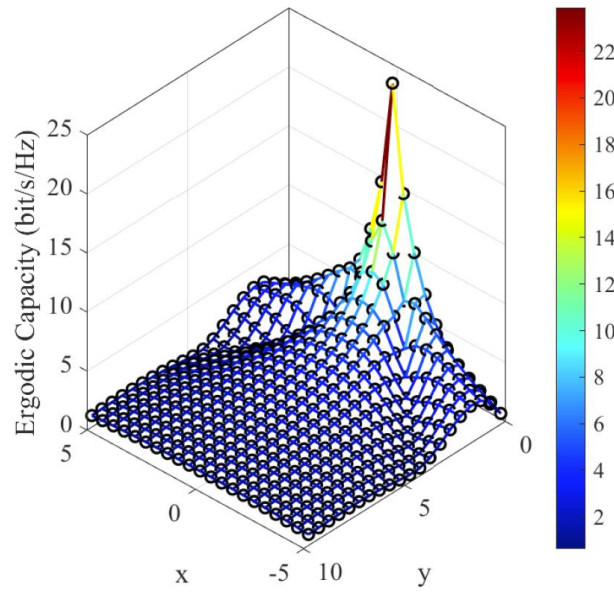


Fig. 4-6 Ergodic capacity distribution in the 10 m  $\times$  10 m square room, for  $\rho_T = 60$  dB,  $\zeta = 0.2$ ,  $\varepsilon = 5.31 - j0.5861f^{-0.1905}$ . Markers represent simulation values while the lines represent analytical values.

The spatial distribution of the ergodic capacity in a square room using our proposed model is shown in Fig. 4-6. It is observed that the ergodic capacity is not a monotonic function of the UE-BS distance. This phenomenon can be attributed to the constructive and destructive interference between the EM waves along the LOS path and the WR path. The length difference in  $O(\lambda)$  leads to the great changes of the amplitude and phase of the superposed EM wave arriving at the UE.

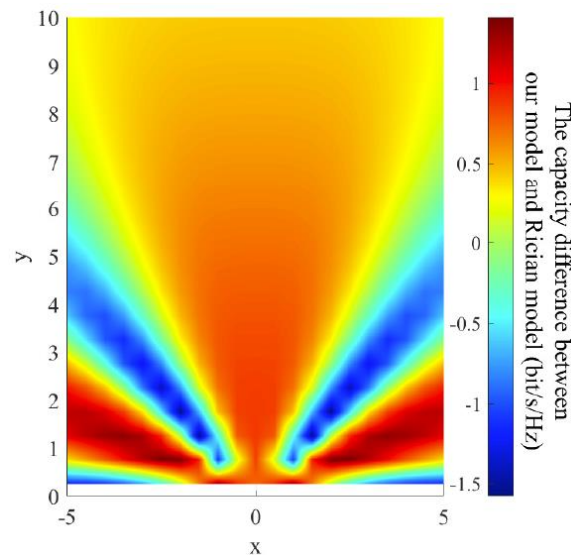


Fig. 4-7 The ergodic capacity difference between our proposed channel and the Rician channel, for  $\rho_T = 60$  dB,  $\zeta = 0.2$ ,  $\varepsilon = 5.31 - j0.5861f^{-0.1905}$ . The positive/negative difference indicates constructive/destructive interference.

Fig. 4-7 plots the ergodic capacity difference between our proposed channel model based on (4.9)-(4.14) and the Rician fading channel model. The position with a positive/negative difference corresponds to a location that experiences the constructive/destructive interference between the EM waves along the LOS path and the WR path. We can see that the positions suffering from the destructive interference appear in certain directions, along which the Fabry-Pérot resonance phenomenon of EM waves is observed.

Concluded from Fig. 4-5 to Fig. 4-7, the impact of the WR path that characterises the EM and physical properties of building materials on indoor ergodic capacity is non-trivial, which cannot be ignored in indoor LOS MIMO communications.

#### 4.4.3 The impact of wall permittivity and thickness on spatially averaged capacity

In order to identify a wall material with desirable wireless friendliness, the relationship between the evaluation indicator named spatially averaged capacity  $C_{\text{avg}}$  and the key parameters, i.e., the permittivity  $\varepsilon_0$  and the thickness  $\zeta$  of building materials is shown in this subsection.

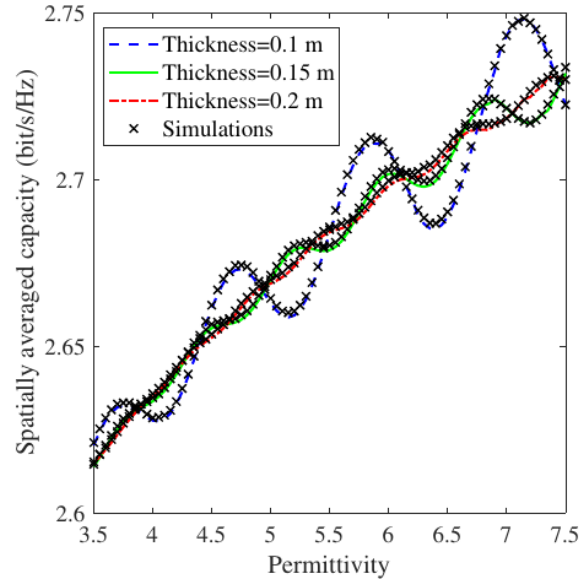


Fig. 4-8 Impact of wall permittivity on spatially averaged capacity for  $\rho_T = 60$  dB.

Fig. 4-8 and Fig. 4-9 plot the spatially averaged capacity as a function of the permittivity and the thickness of building materials, respectively. In Fig. 4-8, as the permittivity increases from 3.5 to 7.5, the envelope of each spatially averaged capacity curve presents an upward trend. The variation in the spatially averaged capacity becomes more significant with the increase of the permittivity.

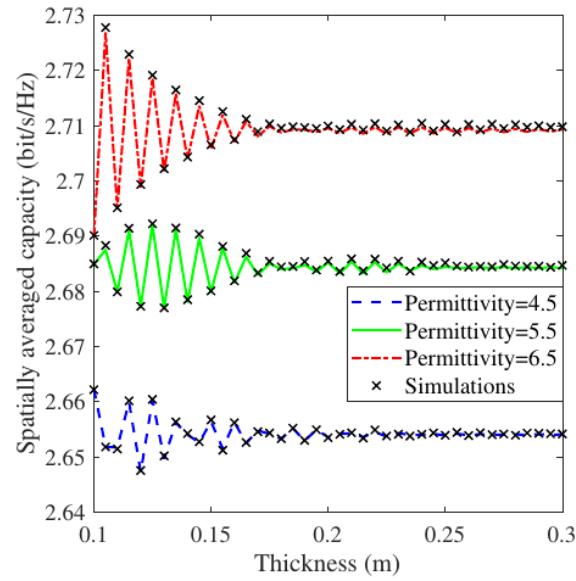


Fig. 4-9 Impact of wall thickness on spatially averaged capacity for  $\rho_T = 60$  dB.

In Fig. 4-9, for a given permittivity, as the wall thickness increases, the spatially averaged capacity first fluctuates with it under a decreasing envelope and gradually converges to a constant value when the thickness goes beyond 0.25 m. We observe quite severe fluctuations of the spatially averaged capacity at relatively small wall-thickness values. That is because the reflection coefficient amplitude fluctuates more severely when the wall is thinner.

From Fig. 4-8 to Fig. 4-9, It should be highlighted that a tiny lapse in the wall permittivity or the thickness would bring about changes in the spatially averaged capacity of up to 0.129 bits/s/Hz.

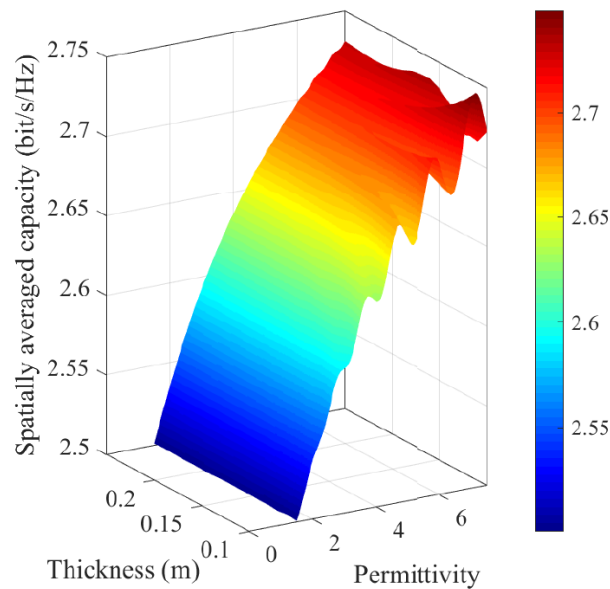


Fig. 4-10 The composite impact of permittivity and thickness on spatially averaged capacity for  $\rho_T = 60$  dB.

The composite impact of the building material's permittivity and thickness on the spatially averaged capacity is illustrated in Fig. 4-10. When the permittivity and the thickness are configured in the range from 1.5 to 7.5 and from 0.1 to 0.25 m, respectively, we observe that the optimal parameter pair of  $[\varepsilon_0, \zeta]$  resulting in the highest spatially averaged capacity of 2.748 bits/s/Hz is [7.15, 0.1], while the worst pair resulting in the lowest spatially averaged capacity of 2.501 bits/s/Hz is [1.50, 0.122].

We can conclude that certain combinations of the wall thickness and permittivity values lead to peak values of the spatially averaged capacity, which can be more than 9.9% higher than the lowest spatially averaged capacity values associated with some combinations of the wall thickness and permittivity values that should be avoided during the selection and/or design of building materials.

#### 4.5 Recommendation

Numerical results demonstrate that building materials as reflectors have to be well selected or designed to avoid the risk of reducing indoor wireless performance, because a minor discrepancy in the configuration of the relative permittivity and thickness of the wall material might cause over 14.4% losses in indoor capacity.

## 5. System-level Mm-Wave Small-cell Simulator based on iBuildNet

### 5.1. Outdoor Environment Modelling

Due to the fact that the environment has a significant impact on the wireless propagation, especially in the mm-Wave frequency band, the outdoor and indoor scenarios shall be modeled close to reality.

We proposed and integrated an Outdoor Layout Module in Ranplan Professional, which supports importing large outdoor scenarios using Geographic Information Systems (GIS) building vectors, clutter, terrain data, and foliage data for the performance evaluations of outdoor and outdoor-to-indoor scenarios. It supports the direct import of geo-data into the Unix-based MSI PlaNET format and this contains:

- Building Vectors
- Terrain Data
- Clutter Data
- Foliage Data
- Projection Information

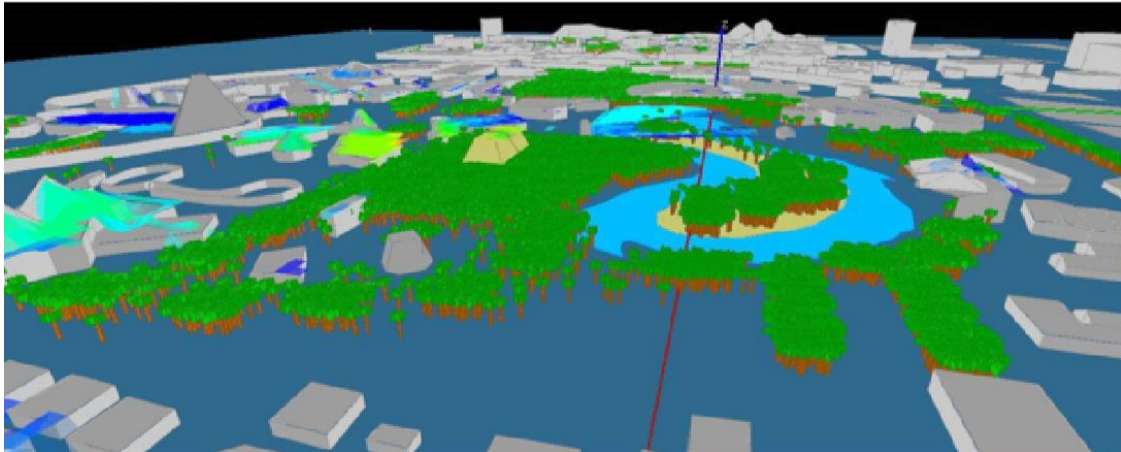


Fig. 5-1. 3D view of an outdoor environment modelling

### 5.2. Indoor Environment Modelling

Same as the outdoor building modelling, the indoor environment modelling need to consider the detailed information including the wall, window, ceiling, chair, shelter, etc.

We provide multi ways of indoor environment importing, such as CAD recognition, Intelligent Floor Recognition (IFR). We also provide a manual way to do the indoor building modelling in case of the missing information within imported file.

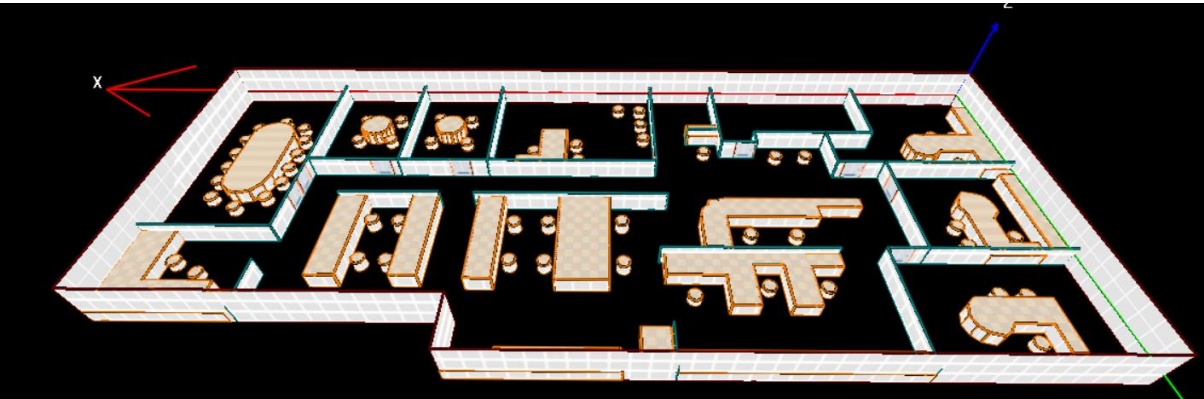


Fig. 5-2. 3D view of an indoor environment modelling

5.3. User Modelling and Traffic Map

Simulation is a critical step in wireless network planning and optimization. To get the accurate simulation results, except the accurate environment model and network modelling, we also need to model the user and the traffic map. When considering the user and traffic map, the simulation can provide accurate performance prediction for the deployment of the system, especially for heterogeneous wireless access networks.

We support to model general user terminal, LTE terminal as well as 5G NSA and 5G SA terminal.

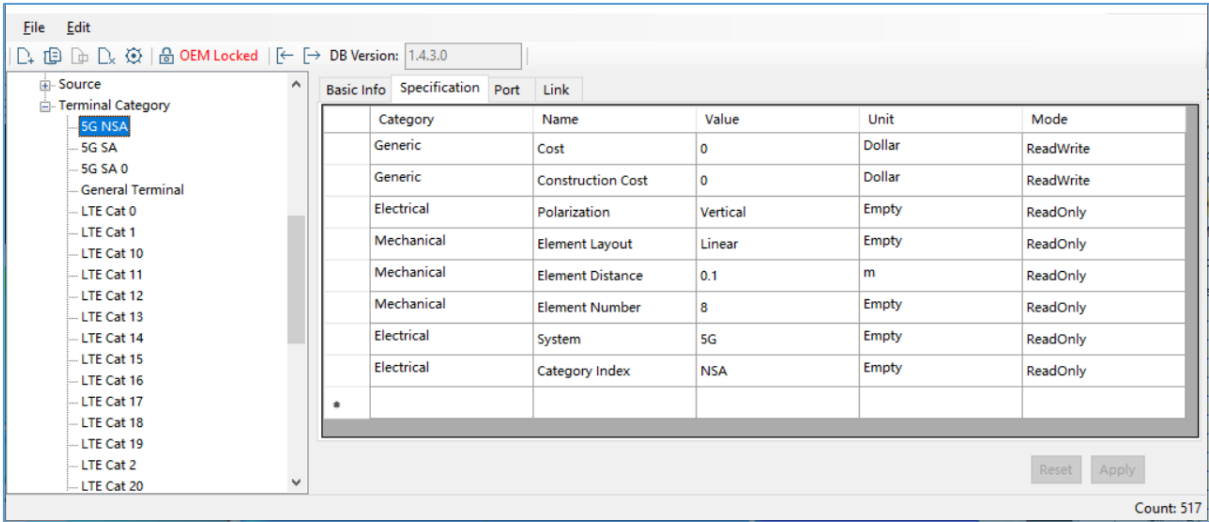


Fig. 5-3. User terminal modelling

We also support modelling the number of users and a traffic map, which includes the type of service, mobility, etc.

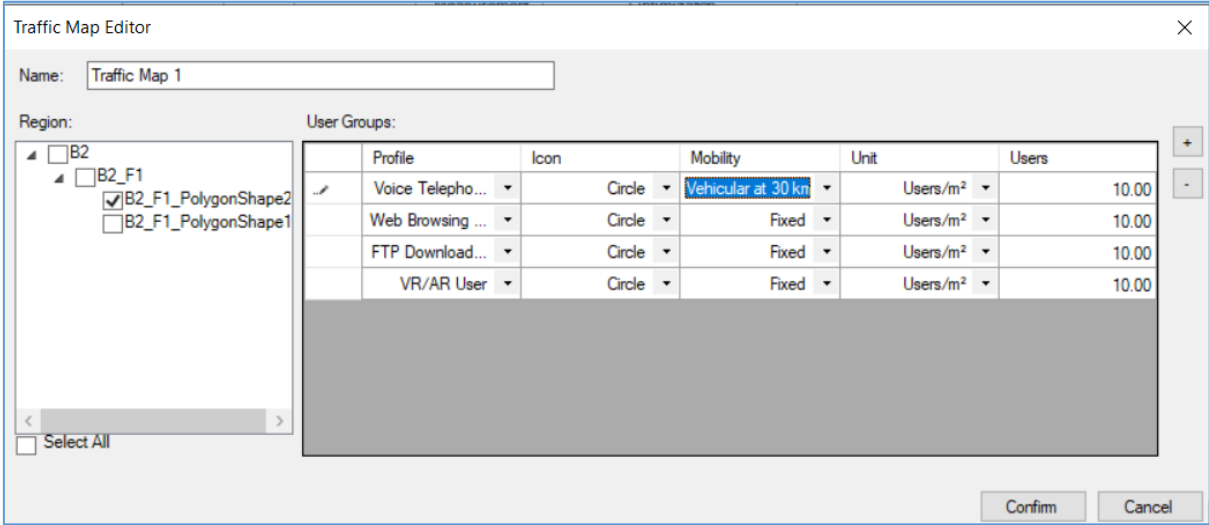


Fig. 5-4. Traffic map

5.4. Simulation Result in Real Scenarios

For the demonstration, the outdoor scenario in a city area is chosen. It has dimensions of 5 km x 5 km. After the GIS data is converted to the supported format, it can be imported to Ranplan Professional. The Import GIS Data window is shown in the Fig. 5-5.

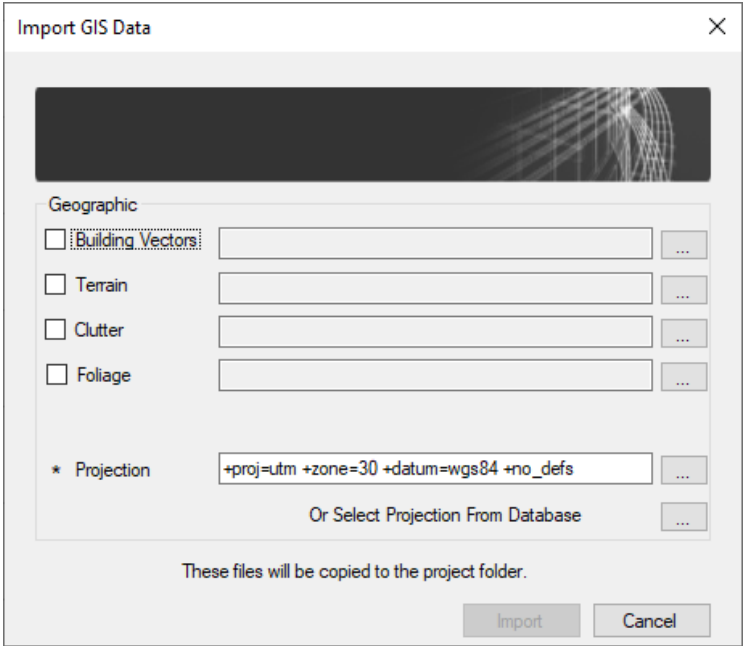


Fig. 5-5. Import GIS Data window in Ranplan Professional

The software can automatically generate the outdoor scenario based on the imported data. The outdoor environment data includes the data of buildings, terrain, and clutter. The 3D view of the imported outdoor scenario is shown in the Fig. 5-6.



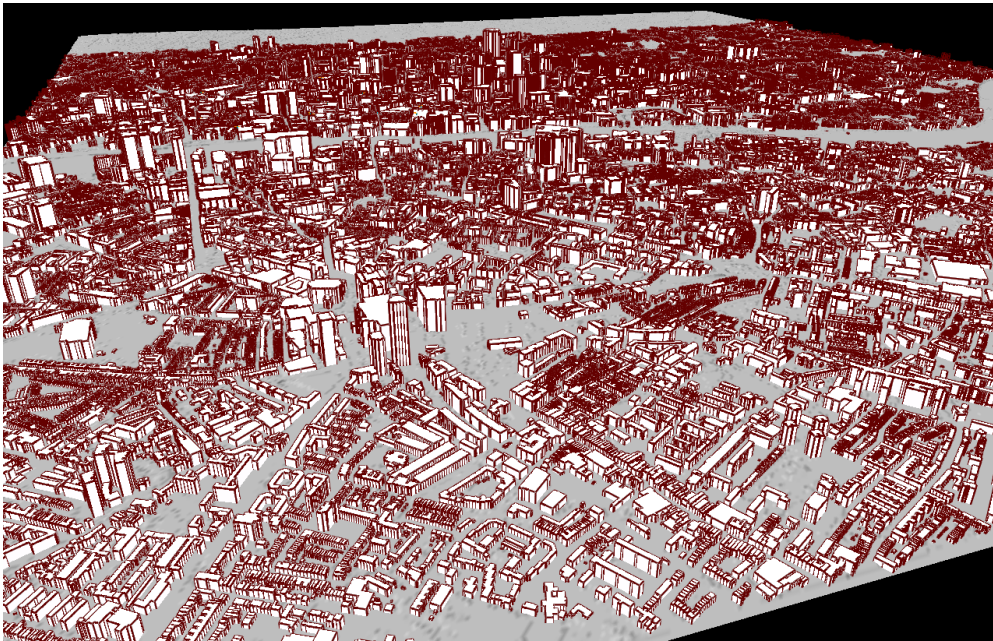


Fig. 5-6. 3D view of the imported GIS data (central London)

At the beginning, we deployed 68 outdoor Macro cells at the top of the outdoor building with the system of 5G NR, frequency band of 3500MHz Band n78, with the band width of 100MHz. The transmission power of the Macro cells is 43dBm. After the network is deployed, we can run various KPIs to test the network performance. The supported 5G NR KPIs is shown in Fig. 5-7. Various KPIs can detailed check the deployed network performance, and user can configure or change the network to improve the network performance.

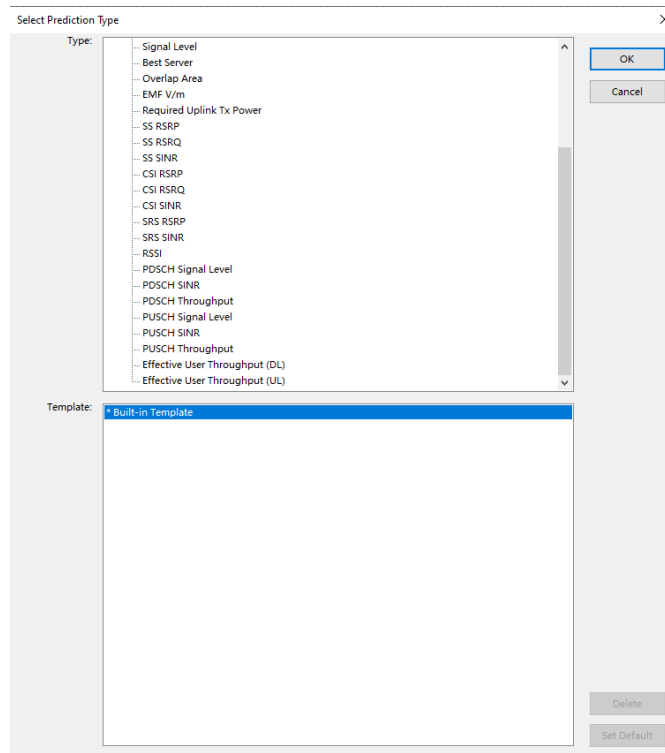


Fig. 5-7. Supported KPIs in 5G NR

The generated KPIs can be check in either 2D or 3D. Two views of outdoor SS RSRP are shown in Fig. 5-8 and Fig. 5-9 for the entire scenario with the same display legend. In 3D view, it provides

the view of SS RSRP distribution and the location of the deployed network devices, providing the convenience for the user to check the network design.

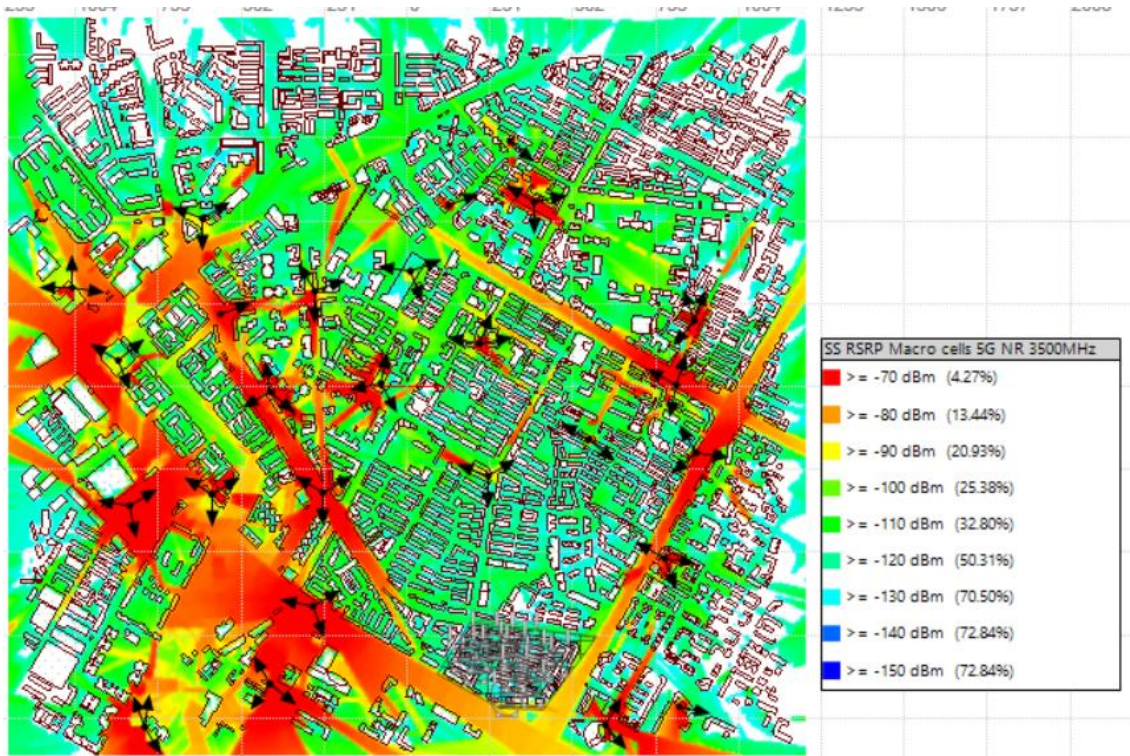


Fig. 5-8. 2D view of outdoor SS RSRP in the whole area

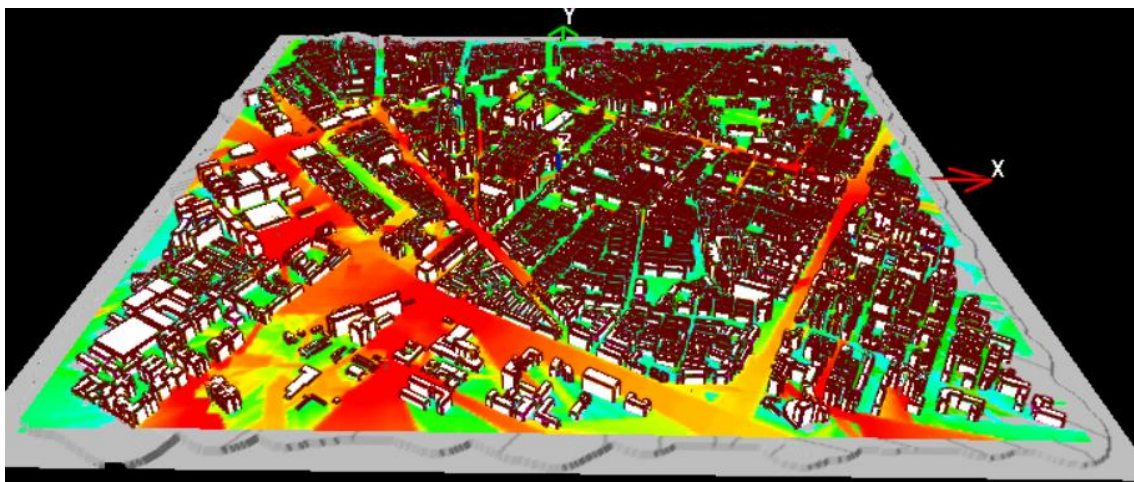


Fig. 5-9. 3D view of outdoor SS RSRP

As can be seen from the simulation results, the Macro cells provide wide and basic coverage, but in some hot points, the Marco cells are hard to provide the adequate signal strength as well as the capacity.

To tackle the issue of weak signa level and provide sufficient capacity to meet the user experience. We deployed 11 Small cells with the system of 5G NR, frequency band of 28000MHz n257, with the band width of 100MHz.

These Small cells are deployed around 10 m height with low transmission power (37dBm). The main purpose of this small cells is to provide optimal signal level within a small coverage area and to offload the capacity from the Macro cell. The SS RSRP prediction in Fig. 5-10 shows the



comparison of performance of SS RSRP in street level when deployed only Macro cells and deployed Macro cell together with small cell in the hotspot area.

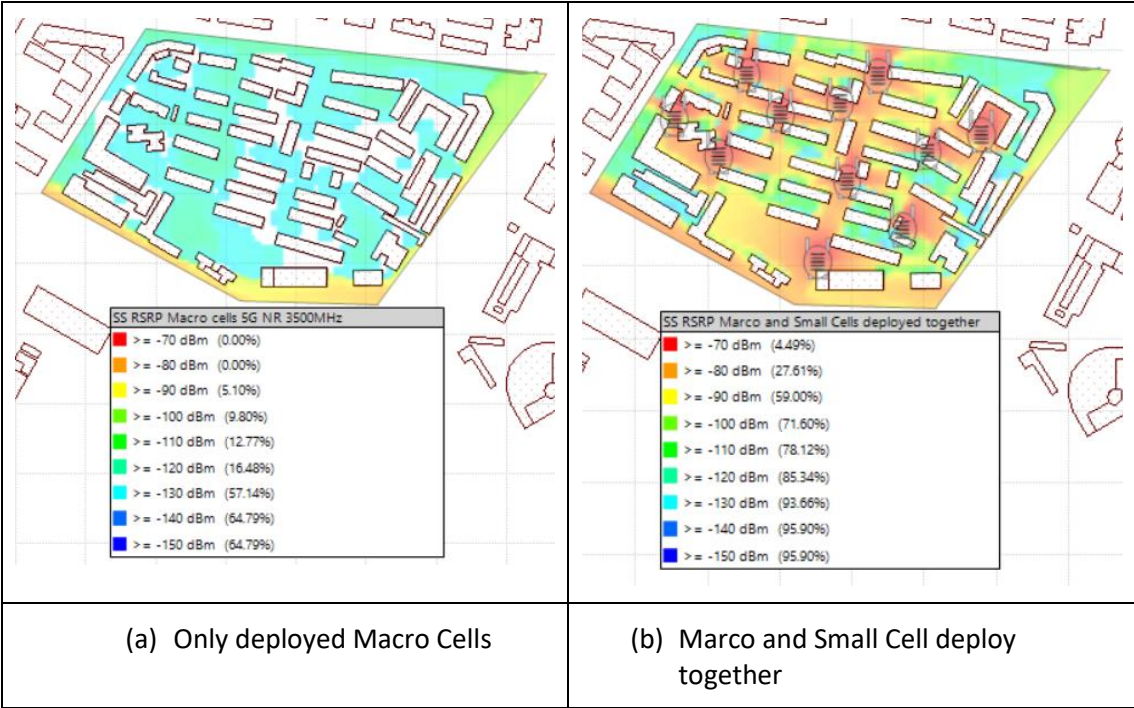


Fig. 5-10. 2D view of outdoor SS RSRP in the hotspots area

We consider there are 30 users in the hotspots area, as shown in Fig. 5-11. There are 10 FTP download users, 10 Full buffer users and 10 Web browsing users. The effective user throughput in Fig. 5-12 shows the comparison of performance of effective user throughput in street level when deployed only Macro cells and deployed Macro cell together with small cell in the hotspots area.

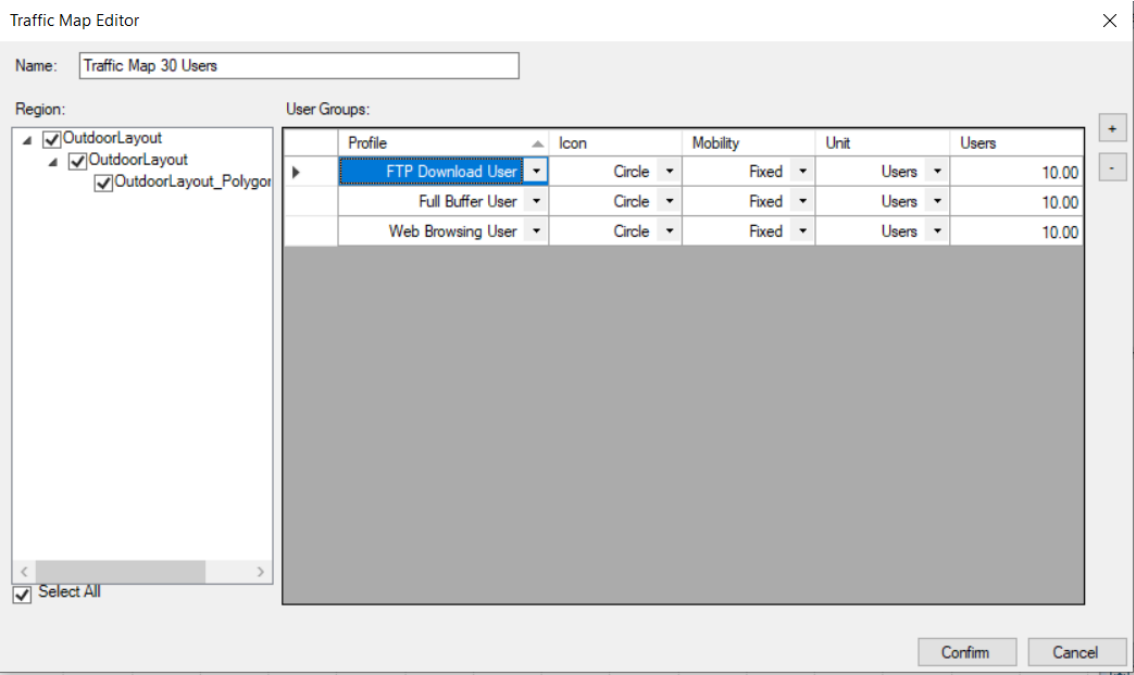


Fig. 5-11. Traffic Map of 30 Users in the hotspots

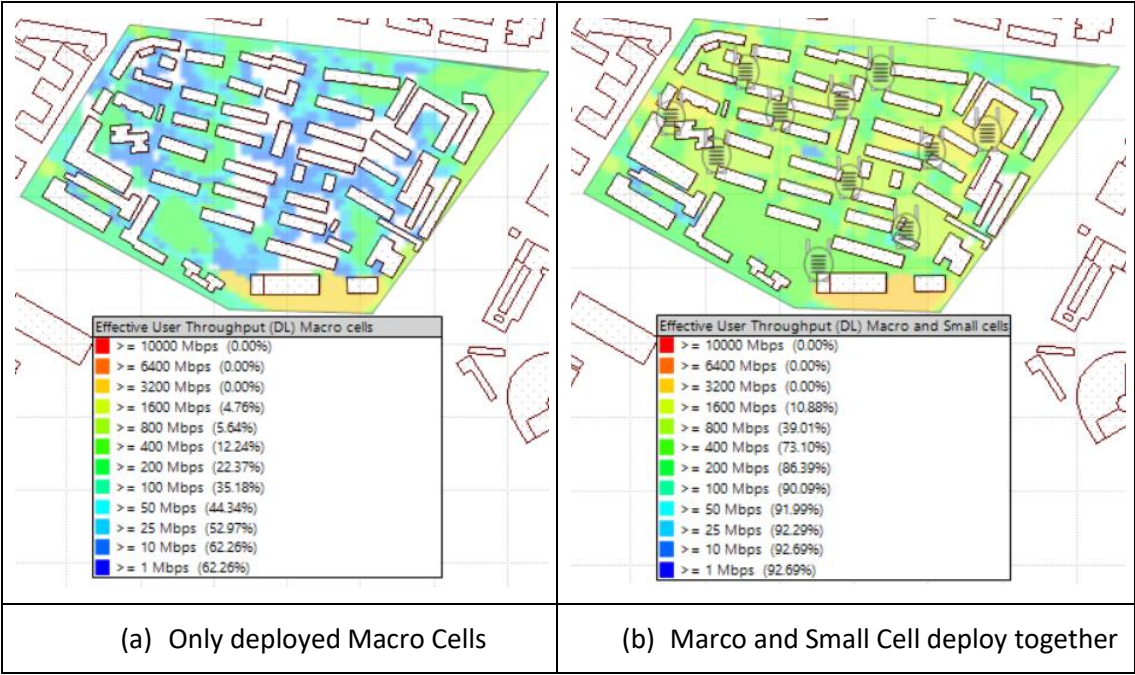


Fig. 5-12. 2D view of effective user throughput in the hotspots area

5.5. Recommendation

In the mm Wave frequency band, by deploying the macro and small cells in the outdoor, a better coverage and capacity can be obtained. Most of the area can be covered by the Macro cells, the coverage blackholes can be eliminated by the small cell, the capacity in the hotspots can be improved by the throughput. Therefore, no matter where the user is stayed, they can obtain optimal signal from the network.

## 6. Sensitivity Analysis of Built Environment Modelling Realism

At millimetre frequencies, the small details that characterize the simulation scenario are critical because of their impact on signal propagation. With wavelengths in the order of tens of millimetres, any roughness of the materials or object would be sufficient to cause signal diffraction. That said, it is essential to model the scenarios as realistically as possible and for this it is necessary to take into account the architecture of the scenario, the distribution of objects on it and the electromagnetic characteristics of the materials.

Moreover, channel models capable of capturing detailed physical and electromagnetic characteristics of the scenario are highly recommended for the millimetre band. In this respect, deterministic models based on ray tracing may be suitable. Ray-tracing techniques consist of launching rays in different directions and evaluating the effect of propagation phenomena on these rays.

For this work, a ray-tracing tool based on the game engine developed at the UPV was used. With this simulation tool it is possible, firstly, to model realistic scenarios and secondly, to obtain a deterministic channel estimation. The channel is estimated taking into account the position and the physical and electromagnetic characteristics of all objects in the scenario. Direct, specular paths up to third order reflections and scattering effects are considered in the simulations.

This study is focused on the sensitivity analysis of the modelling realism for built environments. Specifically, the impact of considering or not the furniture in indoor environments will be evaluated. In addition, the effect of the accurate electromagnetic characterization of the materials on the results is also studied.

### 6.1. Presentation of the Scenario

The environment built in the simulator (Fig. 6-1) is a replica of the meeting room at Durham University presented in Fig. 6-2. The room with the dimensions 8.8 x 5.7 x 3.5 m is set up with the table in the middle, and multiple chairs around it. The walls are built from different materials, glass and plasterboard among them, and there is a carpet on the floor. The same room was described in Chapter 3.

The wideband measurements were conducted with the use of the Frequency Modulated Continuous Wave (FMCW) channel sounder. The Tx horn antenna with 18° HPBW was settled in the corner of the room, and the Rx omnidirectional antenna was moved onto 16 predefined positions around the table. In the Fig. 6-3 the arrow next to the Tx antenna is showing the direction of the horn antenna in the starting position at 0°. During measurements at each of the Rx positions, the Tx antenna was rotated in 15° steps to achieve 24 data sets and complete 360° rotation.

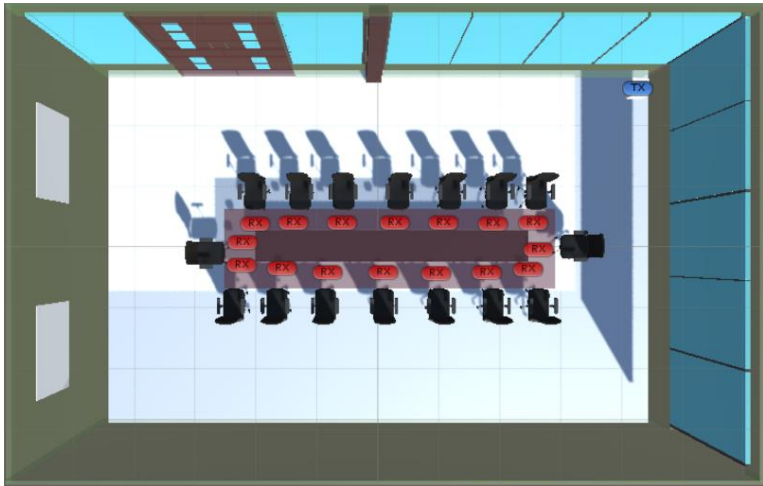


Fig. 6-1. Top view of the Meeting Room created in the simulation tool



Fig. 6-2. Photo of the Meeting Room at Durham University

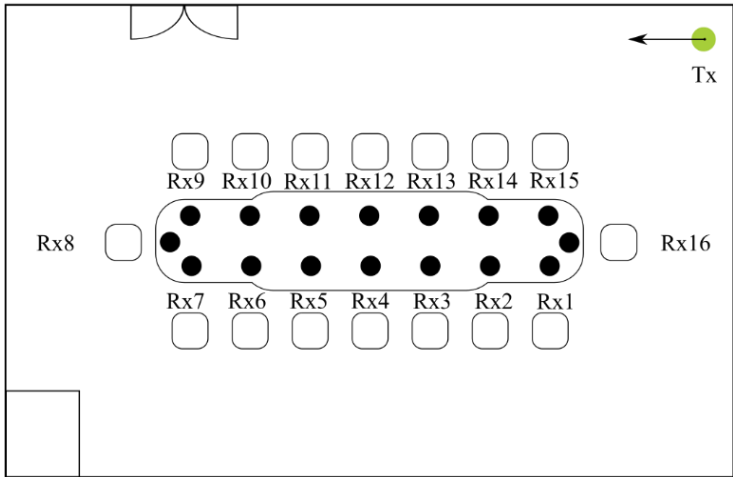


Fig. 6-3. Top view of the Meeting Room with Tx in the corner and Rxs' locations around the table

6.2. Different Accuracy Levels in the Scenario Modelling

In order to assess the impact of modelling accuracy on the results, three scenario configurations are proposed:

**Unfurnished scenario:** The scenario consists only of the physical space itself and the transmitting and receiving antennas. No furniture is considered.

**Furnished scenario (low furniture allocation accuracy):** The scenario considered is similar to the one shown in Fig. 6-1, but the positioning of the furniture is approximated, i.e., The furniture is not in exactly the same position as when the measurements were taken.

**Rough material characterization:** The scenario is equal to the one shown in Fig. 6-1 in appearance, but the electromagnetic characteristics of the building materials are not properly considered. Specifically, all the materials in the room are characterized as glass.

### 6.3. Analysis and Numerical Results

In this subsection, the numerical results are obtained for the scenarios described earlier. For comparison purposes, additionally, the real measurements and simulation results obtained for the scenario with all the furniture in its correct position and the materials characterized are considered.

Fig. 6-4 shows the received power results obtained for each of the 16 transmitter positions and for each of the configurations.

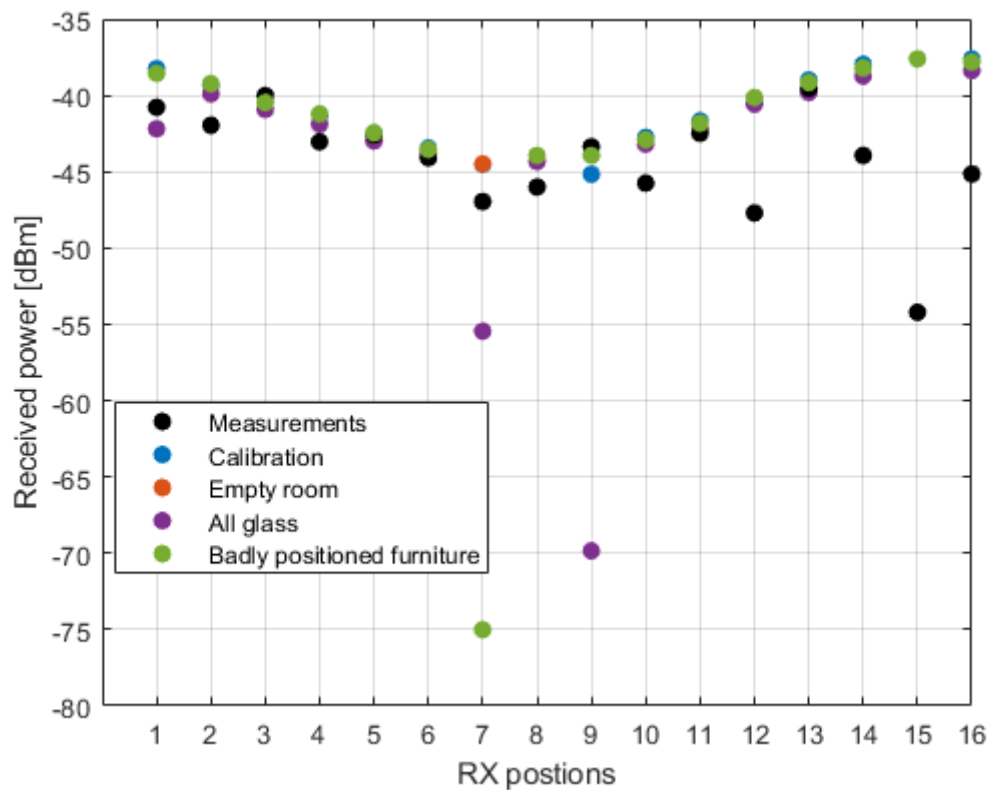


Fig. 6-4: Received power for the 16 RX positions.

As the figure shows, the samples of the real measurements, the calibration and the room with the correctly assigned materials but no furniture ("empty room") are very similar to each other. Specifically, the root mean square error with respect to the real measurements is 28.7942 for the calibration and 26.5161 for the empty room.

In the case of the room with an incorrect assignment of materials ("All glass") and the room with badly positioned furniture, the deviations with respect to the measurements are greater. The mean square error is 74.4102 and 77.2313 for "all glass" and "badly positioned furniture" respectively.

#### 6.4. Recommendation

The above confirms the importance of taking into account both the characterization of materials and the positioning of furniture and objects within the scenario for millimetre frequencies. This fact becomes more relevant in scenarios where there is no direct visibility and therefore the main contributions are due to both specular and scattered reflections.



## 7. Conclusions

In this work, the recommendations on joint optimization of mmW SC deployment and the built environments are presented. They may be helpful in the design of new buildings, furniture renovation, and in future indoor SCN deployments.

For the multi-story building, in the Chapter 2, the coverage probability, and the impact of network density and story height of the SCN was studied. The range of story heights associated with poor network performances was identified. Moreover, it is recommended to use materials with a higher penetration loss for the ceilings, because they can provide better network performance.

In the Chapter 3 the hybrid beamforming's influence on the user rate in a meeting room was presented. We have obtained the optimal locations of small-cells that maximize the sum user rate/minimum user rate through greedy search. The numerical results show that deploying one cell using MMSE precoder provides the maximum sum user rate and deploying two cells operating at different frequency bands using ZF/MMSE precoder provides the maximum minimum user rate.

The recommendation in the Chapter 4 relates to the properties of the materials in the environment. It is crucial to select or designed proper materials as reflectors, because a minor discrepancy in the configuration of the relative permittivity and thickness of the wall material might cause over 14.4% losses in indoor capacity.

In the Chapter 5 the focus is more on outdoor performances, where it is recommended to deploy macro cells, and use SC for eliminating remaining blackholes.

In relation to recommendation from the Chapter 4, in the Chapter 6 it is confirmed that not only material properties are important, but also the furniture positioning. When it is possible, the LoS path should be planned. When it is not possible, the furniture placement may be crucial for obtaining rich multipath propagation.

## References

- [1] M. Ding, P. Wang, D. López-Pérez, G. Mao, and Z. Lin, “Performance impact of LoS and NLoS transmissions in dense cellular networks,” *IEEE Trans. Wireless Commun.*, vol. 15, no. 3, pp. 2365–2380, Mar. 2016.
- [2] M. K. Muller, M. Taranetz, and M. Rupp, “Analyzing wireless indoor communications by blockage models,” *IEEE Access*, vol. 5, pp. 2172–2186, 2017.
- [3] J. G. Andrews, F. Baccelli, and R. K. Ganti, “A tractable approach to coverage and rate in cellular networks,” *IEEE Trans. Commun.*, vol. 59, no. 11, pp. 3122–3134, Nov. 2011.
- [4] J. S. Hygh, J. F. DeCarolis, D. B. Hill, and S. Ranji Ranjithan, “Multivariate regression as an energy assessment tool in early building design,” *Building Environ.*, vol. 57, pp. 165–175, Nov. 2012.
- [5] T. Bai and R. W. Heath, Jr., “Coverage and rate analysis for millimeter-wave cellular networks,” *IEEE Trans. Wireless Commun.*, vol. 14, no.2, pp. 1100–1114, Feb. 2015.
- [6] M. Shafiet al., “5G: A tutorial overview of standards, trials, challenges, deployment, and practice,” *IEEE J. Sel. Areas Commun.*, vol. 35, no. 6, pp. 1201–1221, Jun. 2017.
- [7] A. A. M. Saleh and R. Valenzuela, “A statistical model for indoor multipath propagation,” *IEEE J. Sel. Areas Commun.*, vol. 5, no. 2, pp. 128–137, Feb. 1987.
- [8] X. Yu, J. Zhang, M. Haenggi and K. B. Letaief, “Coverage analysis for millimeter wave networks: the impact of directional antenna arrays,” *IEEE J. Sel. Areas Commun.*, vol. 35, no. 7, pp. 1498–1512, Jul. 2017.
- [9] N. Tafintsev et al., “Improved network coverage with adaptive navigation of mmWave-based drone-cells,” in *Proc. IEEE Globecom Workshops (GC Wkshps)*, Dec. 2018, pp. 1–7.
- [10] W. Wu, D. Liu, X. Hou, and M. Liu, “Low-complexity beam training for 5G millimeter-wave massive MIMO systems,” *IEEE Trans. Veh. Technol.*, vol. 69, no. 1, pp. 361–376, Jan. 2020.
- [11] Huawei, “Five trends to small cell 2020”, Mobile World Congress (MWC), Barcelona, Spain, Feb. 2016.
- [12] J. Zhang, et al., “Wireless energy efficiency evaluation for buildings under design based on analysis of interference gain,” *IEEE Trans. Veh. Tech.*, early access, 2020.
- [13] D. S. Shiu, “Fading correlation and its effect on the capacity of multielement antenna systems,” *IEEE Trans. Commun.*, vol. 48, no. 3, pp. 502–513, March 2000.
- [14] K. Haneda, et al., “Indoor 5G 3GPP-like channel models for office and shopping mall environments,” *IEEE International Conference on Communications Workshops (ICC)*, Kuala Lumpur, 2016, pp. 694–699.
- [15] S. K. Yoo, et al., “Ceiling- or wall-mounted access points: an experimental evaluation for indoor millimeter wave communications,” *13th European Conference on Antennas and Propagation (EuCAP)*, Krakow, Poland, 2019, pp. 1–5.

- [16] C. Jansen, et al., "The impact of reflections from stratified building materials on the wave propagation in future indoor terahertz communication systems, " *IEEE Trans. Antennas Propag.*, vol. 56, no. 5, pp. 1413-1419, May 2008.
- [17] ITU-R, "Effects of building materials and structures on radiowave propagation above about 100 MHz P series radiowave propagation, " *Recomm. ITU-R P.2040-1*, Jul. 2015.
- [18] Y. Zhang, et al., "How friendly are building materials as reflectors to indoor LOS MIMO communications?, " *IEEE Internet Things J.*, vol. 7, no. 9, pp. 9116-9127, Sept. 2020.
- [19] M. B. Zetterberg, et al., "IST-2003-507581 WINNER D5.4 v1.4 final report on link level and system level channel models, " Nov. 2005.
- [20] G. Alfano, et al., "Mutual information and eigenvalue distribution of MIMO Ricean channels," *Proc. IEEE Int. Symp. Inf. Theory Appl. (ISITA)*, Parma, Italy, Oct. 2004, pp. 1-6.
- [21] A. Maaref and S. Aïssa, "Capacity of MIMO Rician fading channels with transmitter and receiver channel state information, " *IEEE Trans. Wirel. Commun.*, vol. 7, no. 5, pp. 1687–1698, May 2008.
- [22] M. Alouini and A. J. Goldsmith, "Capacity of Rayleigh fading channels under different adaptive transmission and diversity-combining techniques, " *IEEE Trans. Veh. Technol.*, vol. 48, no. 4, pp. 1165-1181, Jul. 1999.